CHALMERS

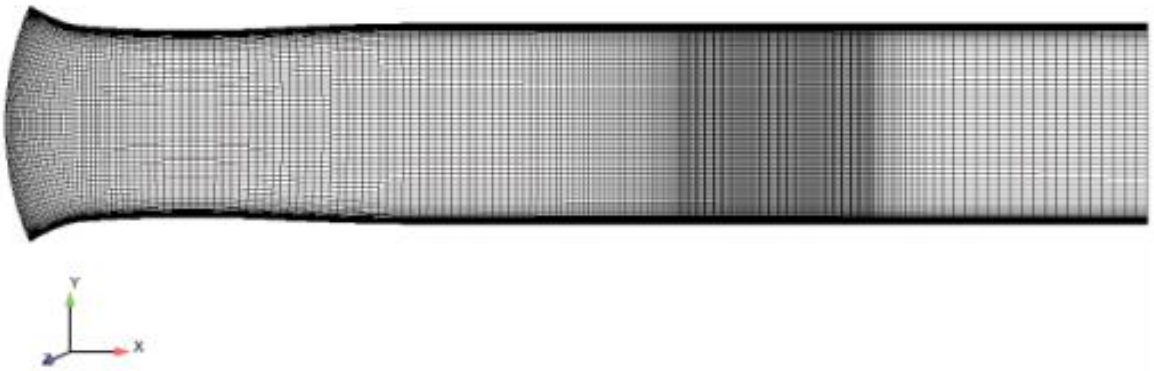

Numerical Investigation of 3D Compressible Duct Flow
with Shock-Wave/Turbulent Boundary-Layer Interaction

Master of Science Thesis in the Program Mechanics of Solids and Fluids

MARTINA BLOM

Chalmers University of Technology
Department of Applied Mechanics
Göteborg, Sweden, July 2010

Numerical Investigation of 3D Compressible Channel Flow with Shock-Wave/Turbulent Boundary-Layer Interaction

MARTINA I. M. BLOM

Examiner: LARS DAVIDSON

Chalmers University of Technology
Department of Applied Mechanics
Division of Fluid Dynamics
SE-412 96 Göteborg
Sweden
Telephone +46 (0)31 772 14 04

Cover:
Computational grid used for Mach number 1.3. Please see page 25 for further details.

Department of Applied Mechanics
Göteborg, Sweden, July 2010

Abstract

A generic supersonic bump flow in a duct has been studied. The flow over the bump is accelerated, inducing a shock wave in the downstream, interacting with the wall boundary layer and triggering boundary layer separation. Two Mach numbers, $M = 1.3$ and $M = 1.4$, are considered in the present computations, by which the effects of weak and strong wall boundary conditions have been explored. The bump flow has been a test case for RANS and hybrid RANS-LES modelling verification specified in the European Union project ATAAC (Advanced Turbulence Simulation for Aerodynamic Application Challenges, 2009-2011). In this thesis work, several RANS turbulence models have been tested using the FOI CFD solver, Edge. One of the main purposes is to investigate the effect of turbulence modelling on the predicted flow features in comparison with available experimental data.

With different RANS models, a large part of the work has been dedicated to the investigation of shock-wave location in association to the back pressure specified at the outflow section of the duct. Along with the predicted shock position, pressure and velocity profiles have also been compared to experimental data. Moreover, cross comparisons have been made using the results obtained with various turbulence models. Some previous studies using RANS modelling have highlighted that, in spite of symmetric geometric and flow conditions, the predicted flow may become asymmetric at Mach numbers $M = 1.4$ and larger, e.g. $M = 1.5$. Such an unphysical behavior has been attributed to different (and rather tentative) explanations in terms of turbulence modelling and related numerical issues. The present computations are expected to serve as part of a comprehensive investigation, with further understanding of the flow physics and its numerical modelling.

Acknowledgment

I would like to thank my examinator Prof. Lars Davidson for cheerfully guiding me through this master thesis work. Always keeping his door open and patiently discussing any concerns he has added not only valuable input of knowledge, but also been a source of inspiration and motivation. Truly showing faith in my work, he has really encouraged an independent approach to the work from my side.

Also, I would like to thank my supervisor, Prof. Shia-Hui Peng, for providing expertise advice on the Edge software and turbulence modeling. Moreover, tireless seeing to the progress of the project and spending vast amounts of time on supervising me, I really felt the engagement from Shia-Hui, despite the project being on a mere master thesis level.

Finally, I would like to thank Sebastian Arvidsson (PhD student) for providing me with empirical knowledge on how to use the Edge software and always answering my questions when struggling with the computer. Despite being very busy with his own PhD studies, he always found time to help me out of my concerns.

Contents

1 Introduction

The interaction of a turbulent boundary layer and the shock wave arising in a duct is the main topic of the present investigation. Different turbulence models together with the Edge CFD code are assessed. For the set-up of the flow case, convergent-divergent nozzle liners of various geometries have been used to vary the free stream Mach number of the test section according to specifications. Previously, this case has been experimentally investigated by Bruce and Babinsky [1] for three different flow conditions, $M = 1.3$ and $Re_{\delta^*} = 14770$, $M = 1.4$ and $Re_{\delta^*} = 13600$ and $M = 1.5$ and $Re_{\delta^*} = 13000$, where Re_{δ^*} is the Reynolds number based on the displacement thickness δ^* and M is the Mach number. Additionally, extensive numerical studies of this flow field using RANS, hybrid LES/RANS and LES [2] have been accomplished within the UFAST project [18]. The flow case at hand has been very challenging indeed to CFD computations due to difficulties in capturing certain flow features. Those include the phenomena of unsteady interaction of the shock wave with the boundary layer and subsequent shock-induced separation, as well as the secondary separation bubbles in the corner. In steady mode and for $M = 1.4$ and $M = 1.5$, RANS and URANS solutions, based on the Spalart-Allmaras model for example, have proved asymmetric. Further research has suggested the cause of the asymmetric solutions being the inability of turbulent models invoked to accurately predict corner flow separation, as well as to reasonably represent the physics of the evolution of the shock wave and its interaction with the turbulent boundary layer.

2 Purpose

The general objectives of this Master Thesis project have been twofold; to carry out a literary review of the current state-of-the-art of studies on the interaction of Shock Wave and Turbulent Boundary Layer (SWTBL) and to understand and use the Edge solver in computations of the compressible bump flow, which is a test case for the EU project ATAAC [20]. More specifically, the major purpose of this thesis work has been to investigate the performance of some turbulence models, as well as the effect of boundary conditions, in the prediction of the turbulent bump flow in a duct subjected to SWTBL interaction and flow separation and, consequently, to better understand the flow physics for improveing its CFD modelling.

3 Theory

3.1 Internal transonic flow

Two-dimensional flows have been chosen in many cases for modelling verification of internal turbulent flows, due to a simpler experimental investigation and substantially lower computational cost. However, such an approach might overlook the impact of end-wall effects and thus some of the interesting turbulent features. Therefore, for this very investigation, no two-dimensional solution was aimed at before starting the three-dimensional simulations, as that would probably not have yielded a reasonable initial solution anyway. Additionally, previous research within the area of Shock Wave-Turbulent Boundary Layer Interaction (referred to as SWTBLI hereafter) has erroneously been constrained by the belief of poor two-dimensional flow predictions implying poor three-dimensional solutions [19].

The flow field to be predicted here is that of subsonic inlet flow accelerating over a bump and reaching supersonic conditions, namely $M = 1.3$ or $M = 1.4$ depending on what geometry is being used. A shock wave is formed downstream of the bump, with its exact location depending on the back pressure as specified in the boundary condition file for the outflow section of the duct.

3.2 Shock Wave - Turbulent Boundary Layer Interaction (SWTBLI)

3.2.1 Introduction

The phenomenon of interaction between a shock wave and a turbulent boundary layer is currently not very well understood. Associated features are those of shock induced separation of the boundary layer and high and low frequency shock movements. Both experimental and numerical research has been done on the matter over the past decades, yet without any significant break-through, when it comes to understanding the fundamental flow physics behind such phenomena. Currently, there is great interest in explaining low frequency unsteadiness observed in SWTBLI:s, not the least because of its practical implications on internal and external flow fields in aircraft dynamics. Typically, such low frequency oscillations are found to be a couple of magnitudes smaller, than those normally associated with the upstream free-stream velocity and the boundary layer thickness. At present, the underlying causes of the low frequency shock

movements is not well known, although various explanations have been proposed [3]. These include the impact of upstream features of the incoming turbulent boundary layer [4] and, recently, also some intrinsic mechanisms having an impact [22].

3.2.2 Shock motion and impact of upstream flow conditions

A combined theoretical and experimental investigation by Narayanswami et al. [6] describes the general difficulties faced when simulating flows with SWTBLI:s. The complex flow structures generated within the interaction region together with the substantial non-uniformities observed in the outflow are emphasized. Flow at $M = 8.3$ with crossing shock waves from two symmetric sharp fins mounted on a flat plate are simulated, using the Baldwin-Lomax algebraic turbulence eddy viscosity model. Whereas predictions of surface pressure and flow patterns agree fairly well to those of experimental results, the surface heat transfer is greatly over-predicted. The authors attribute these inconsistencies to the limitations of the turbulence model and call for the need for further development of turbulence models for the prediction of surface quantities, such as heat transfer, complex viscous-inviscid interaction flows. The streamline interaction structure, according to the simulations, consists of two weakly counter-rotating vortices from individual SWTBLI:s from each fin, combined to form a low total pressure jet. The interaction of the individual shocks from the fins, together with the collision of associated helical separation vortices at the center-line, is believed to be the cause of the complex wave structures in the interaction region. Further, large-scale flow separation and a significant loss in total pressure are thought to cause considerable non-uniformities in the outflow.

The region between the inviscid free stream and the turbulent boundary layer has been investigated by Davidson [5] for transonic flow in a plane duct with a bump. A second-moment Reynolds Stress Transport model accounting for physical phenomena, such as streamline curvature, strong non-local and history effects and large irrotational strains has been shown superior to $k - \epsilon$ models, when it comes to physical (but not necessarily numerical) accuracy. It is pointed out, that $k - \epsilon$ models cannot account for normal stresses but randomly compensate for this by over-predicting the shear stresses. However, $k-\epsilon$ models generally lack predictive capabilities for flows involving large normal stresses. Additionally, observations of shock movement from the corresponding experimental investigation lead to suggestions of unsteady methods, such as

LES (Large Eddy Simulations), being used for further investigation of the flow case.

Nevertheless, no large-scale shock movement is seen for the investigation by Wollblad, Davidson & Eriksson of transonic flow across a 2D bump using well-resolved LES [21]. Here it is concluded, that large-scale shock motion might not be a local phenomenon. Thus it actually might be created by disturbances in experimental facilities and therefore not observed for these LES simulations. Another possibility mentioned is the risk of resonance between the shock and distant parts of the flow not included in the present simulations but still causing the large-scale shock motions observed by other authors. Further, the problem of LES being too expensive for being employed with the large domains necessary for confirming such conjectures is pointed out.

An experimental investigation of an impinging oblique shock wave on a turbulent boundary layer at $M = 2.3$ is presented by Debieve and Dupont [22]. A strong unsteadiness is observed for the place of interaction, with frequency ranges extending over two orders of magnitude. A link is drawn between low frequency shock movement and features of the separation bubble, especially phase relationships. On this basis, a simple scheme for streamwise evolution of instantaneous pressure is proposed, building mainly on pressure signals from within the shock oscillation region. As this corresponds to a focus on intrinsic properties having a major impact on the features of the SWTBLI, the method is believed to be relevant also for other shock-induced separation phenomena, such as compression ramps, blunt bodies, over-expanded nozzles. More specifically, the results presented show a strong relationship between the shock foot and the second part of the separation bubble, where a phase opposition was seen especially with the reattachment zone regardless of shock strength. Pressure fluctuations due to shock movement are observed to occur with a negligible time delay relative to the shock time scale, and taking the reattachment zone into consideration make them nearly simultaneous. Thus the relation between pressure fluctuations and shock movement is considered as quasi-instantaneous, i.e. faster than acoustic propagation and streamwise convection. In contrast, no coherence was observed with the incoming turbulent boundary layer.

In comparison, Lee [7] describes how conical symmetry is observed for the interaction flow field far from the fin leading edge. The interaction arises as an equilibrium turbulent boundary layer on a flat plate is allowed to interact with swept planar shock waves. Moreover, topological features of the interaction flow seem to stem from a virtual conical origin far upstream of the interaction region.

Previously a scaling law [8] for sharp-fin interactions has been suggested and in Lee's work it is re-examined for different Mach number flows. The scaling law seems to be in accordance to Lee's experimental results but it is pointed out, that application of the law by simply extending the conical asymptote of the upstream influence line is not appropriate for finding the location of the virtual conical origin. Instead surface streak-line patterns from kerosene-lampback tracings are used for identifying the virtual origin, upstream influence etc.

Also in opposition to the findings by Debieve and Dupont [22], the investigation by Touber and Sandham [23] indicates a linear relation between the the relative interaction length and the oblique shock strength if scaled with the boundary layer thickness and the wall shear stress respectively. Three different LES models are used for this study of the interaction between an oblique shock wave and a supersonic turbulent boundary. The three relevant flow cases are covered in the UFAST project, including experiments at the "Institut Universitaire des Systèmes Thermiques Industriels" in Marseilles, France, (IUSTI), the "Institute of Theoretical and Applied Mechanics" in Novosibirsk, Russia, (ITAM), and the "Aerodynamics Laboratory, Faculty of Aerospace Engineering", Delft University of Technology in Delft, Netherlands, (TUD). The interaction length considered was defined as the distance between the theoretical inviscid shock impingement point and the mean position of the reflected shock. A linear relation was observed even when using the extension of the separation bubble as a measure of the interaction length but the line was then displaced to the right in the graph. These results are in accordance with previous experimental results [24]. For all cases, the same inflow technique is used in order to avoid possible low frequency interferences with the shock-boundary layer interaction, so as not to force any particular low frequency shock movement. The computational domains used are fairly wide, comprising 1.2 to 2.2 times the length of the separation bubble. In addition, the results are integrated more than 25 times the period of the most commonly reported low frequency shock oscillations, so as to allow time-averaged, low frequency dynamic level comparisons. Worth mentioning is that the separation bubble is very shallow for the tested configuration and does not exceed the incoming buffer layer. The magnitude of the mean reversed flow is observed as being less than three percent of the free stream velocity at all times.

3.2.3 Flow control applications with SWTBLI:s

Flow control of SWTBLI forms another significant aspect in studies of SWTBLI flow physics. Blinde et al. [9] has investigated the effects of micro-ramp sub-boundary layer vortex generators on incident SWBLI at $M = 1.84$. The results seem quite promising as the micro-ramps here have a stabilizing effect on the shocks by reducing their motions by approximately 20% as measured in the lower measurement plane. The micro-ramps are observed to generate packets of individual vortex pairs downstream of their vertices. These vortices then act, in a time-averaged view, as counter-rotating longitudinal streamwise vortex pairs perturbing the incoming boundary layer. Low speed regions are observed downstream of the ramp vertices with high speed regions at intermediate locations. Additionally, the vortex pairs seem to enhance the spanwise variation of flow properties, i.e. mixing across the surface of the boundary layer. In the sense of flow control, the presence of the ramps reduces the probability of reversed flow by 20% and 30% for single and double row configurations of the ramps, respectively.

Correspondingly, Kontis et al. [25] attempt to control the SWTBLI:s in an experimental investigation. Dimples are used for a type of passive flow control over a series of hemi-cylindrically blunted fins at different Mach numbers and angles of sweep. Indents are drilled across the hemi-cylindrical leading edge at different angles and the effect of the dimples on the SWTBLI is not a symmetric one. On the upper side, the oblique shock strengthens, so increasing the scale of the interaction, whereas on the lower side, the shock wave is altered in shape and size as compared to the case where no dimples are used. Also, the dimples prevent the shock wave from moving too far downstream, which means a reduced shock movement and a delay of buffet onset. The interactions are believed to depend on properties at the fin leading edge, the side wall and the local boundary layer thickness. Thus it is concluded that dimples affect the local flow field around the leading edge and so alter the effective geometry in the leading edge region. Nevertheless, the authors stress the importance of further research on the effect of dimples on flow control and the underlying flow physics.

3.2.4 Current state and future concerns of SWTBLI:s

Obviously, flow control of SWTBLI is of practical use in order to suppress shock-induced flow separation, by which some underlying SWTBLI flow physics can also be explored. Consequently, many studies have indicated the need for

further research so as to understand the underlying principles in addition to mere empirical observations. Such understanding would certainly enable better flow control of SWTBLI for industrial applications, but also serve an improved flow-physics modelling in simulations of SWTBLI.

Dolling [19] has highlighted current issues as well as priority areas of research concerning SWTBLI. The important implications of the phenomenon on high-speed flight performance and vehicle aerodynamics are pointed out, and the potential industrial applications of related research in progress are highlighted. Further, the main problem areas identified until present date comprise those of accurately predicting peak heating in strong interactions, predicting unsteady pressure loads and explaining the essential physics behind the observations. Even though progress in computational and experimental methods and equipment is acknowledged, this is believed to be accompanied by more demanding vehicle missions and construction constraints, harsher flow regimes and increasing need for flow control. Thus a deeper understanding at all levels will be required. Additionally, it is claimed that the tools for analysis actually available today are not fully utilized, thus rendering a slower progress than might otherwise be. Concrete suggestions for areas of focus concerning SWTBLI involve firstly Large Eddy Simulations, where particularly unsteady behavior and the prediction of unsteady thermal and pressure loads should be prioritized. Secondly, heat transfer prediction requires better measurement techniques, as well as an understanding of the reasons behind the extremely poor predictive capabilities of strong interactions. Thirdly, understanding the causes of the large-scale, low-frequency pulsation of separated flows is stressed. This implies a minimum of realizing whether the phenomenon is an inherent feature of the SWTBLI or rather caused by conditions prevailing exclusively in a wind tunnel environment. Fourth, the interactions where an incoming boundary layer is developing in a pressure gradient need to be evaluated so as to judge whether they are yawed or fully three-dimensional. Fifth, transitional interactions are of great importance, as is finally flow control. According to Dolling [19], the most profitable approach for enhancing the progress in the field would be coupled numerical and experimental work. This has been demonstrated by a number of previous studies, for example, by Gaitonde et al. [26]. They solve the 3D Navier-Stokes equations using a $k-\epsilon$ model to represent the effect of turbulence for a double-fin arrangement at $M = 4$. The computation has generated details of the shock structure, the vorticity field and flow field evolution with increasing interaction strength, that could not have been obtained experimentally [19]. Recently, Schmisseur

and Gaitonde [27] extended their work to even stronger interactions. Similarly, the AGARD working group 18 [28] has investigated current numerical capabilities, regarding both laminar and turbulent interactions, in high speed vehicle aerodynamics. As expected, tools for predicting aerodynamic and thermal loads are available with current grids. Also, for turbulent flows, pressure distributions in three-dimensional interactions are quite accurately computed with little deviation between different turbulence models. This is explained by an approximate triple deck structure of such flows, with a thin inner layer adjacent to the wall, a second deck comprising most of the boundary layer and a third deck above the boundary layer. For the inner layer, both viscous and turbulent stresses are present but even heat transfer and inviscid effects play a major role. Continuing to the second deck, the flow is inherently rotational and inviscid, whereas for the third deck, the flow is mostly irrotational and inviscid. It is further claimed that surface pressure, to a first approximation, is a result from the interaction with the second and third decks and thus not much affected by the choice of turbulence model. In contrast, the skin friction coefficient and the heat transfer distribution are generally poorly predicted and thus highly dependent on the turbulence model used. Moreover, primary separation might be rather well predicted whilst secondary is normally not. Another interesting feature is the poor predictive capabilities for two-dimensional interactions surmounted by those for three-dimensional flows, in which the mean flow quantities cannot be accurately predicted. Note that steady RANS computations are not able to account for unsteady effects and, moreover, the use of a single length scale in eddy-viscosity models is often awkward when modelling turbulent separated flows. This is because such flows comprise several length scales of different magnitudes. For demonstration, Knight and Degrez [28] have shown that eddy viscosity models lose their validity even for two-dimensional flow separation and reattachment.

A further argument raised is the implication of a truly accurate simulation generating time histories for all variables, not only the few ones measured. Such information might then be used to understand the role of three-dimensional effects on separated flows and the downstream regions, the suppression of turbulence in large-scale, separated flows, whether re-laminarization occurs or not, the effect of suppression and augmenting of turbulence due to shock waves, compression waves and expansion fans and finally the causes of flow field unsteadiness in SWTBLI:s. These are only examples of questions lacking a satisfying answer at present and were all raised in the detailed experimental study by Zheltovodov [29]. Despite the limitations of RANS methods when it comes to heat transfer

predictions and fluctuating loads, it is believed that RANS approaches could still be used for certain design purposes, as the mean pressure distribution and the primary separation might be fairly well predicted with RANS. In contrast, it is pointed out that LES for compressible flows, especially those involving SWTBLI:s, is still a rather new field. However, some substantial progress of LES capabilities is likely to have occurred since the time of this review [19] nine years ago, as is demonstrated in some more recent investigations referred here [21].

3.3 Boundary conditions

In numerical computations strong wall boundary conditions are usually implemented, in which constant wall boundary values of unknowns are specified and directly used. This means that those specified wall values are not taken as unknowns in the solution. Alternatively, weak wall boundary conditions are also applicable, in which the solution is looping over the wall boundary nodes and driving the boundary value approaching its actual value (which would otherwise be specified in strong wall boundary conditions). Ideally, the weak and strong boundary conditions should be identical, provided that the solution is sufficiently converged and the grid resolution is fine enough. In practice, very small differences may be observed in the computed wall values, but they should hardly impose any effects on the predictions, since the actual wall flux is often ensured with weak wall boundary conditions for flow and turbulent quantities. Obviously, the use of strong wall boundary conditions is more straightforward by invoking directly the actual wall values of unknowns in solution. Nonetheless, for many cases the solution convergence may become more robust by using weak wall boundary conditions. The boundary conditions used in the present investigation are described briefly below.

3.3.1 Wall boundary conditions

For Edge, three different wall boundary conditions exist; Euler, adiabatic and isothermal ones. For viscous flows, the most common is adiabatic wall, which is also the case for the computations in this investigation. The original type of adiabatic wall is a strong formulation, specifying the velocity at the wall normally through the no-slip condition, as is done here. For an adiabatic wall, both the density and the energy equation have zero boundary flux imposed on them, i.e. weak boundary conditions. Also the second type of viscous boundary

condition, the isothermal one, uses a strong approach for the velocity at the wall whilst employing a weak condition on the constant wall temperature. In contrast, an Euler boundary condition can only be applied to inviscid flows and is also a weak condition, thus imposing itself through the flux.

Turbulent variables are specified as strong and by default a wall resolved grid is considered with $y^+ \approx 1$ in the first layer of nodes outside the wall, with

$$y^+ = \frac{y * u_\tau}{\nu} \tag{1}$$

where y is the wall distance (of the first node) and u_τ is the wall skin-friction velocity.

Nevertheless, wall functions might be used where larger values for y^+ could be specified for the first computational node. Notably, wall functions are not used for this case as the grid is sufficiently fine all the way to the wall.

3.3.2 Weak versus strong wall boundary conditions

Previously an investigation of the differences in the solutions using strong as compared to weak wall boundary conditions has been performed [18]. The model problem is that of a linear advection-diffusion equation for a boundary layer problem. It is shown that the weak solution converges to the strong solution in the limit of vanishing grid size or large penalty parameters. For a second order scheme and a coarse mesh, the weak solution seems more accurate, as is also the case for the full Navier Stokes and a coarse mesh. For fine meshes, the strong solutions were in general more accurate.

3.3.3 Total States Inlet (Weak Total States)

Setting this boundary condition, total pressure, total temperature and a flow direction are specified at the inlet boundary, in this case the duct opening. The Mach number is then extrapolated upstream. This boundary condition was constructed for subsonic inflow conditions of internal flow. However, it is possible to also specify local varying free stream data at the inlet boundary. Dependent variables, such as turbulence intensity, could be specified and will be used in that case. Just for the sake of interest, the Total States Inlet boundary condition also exists in a strong formulation, for which the static pressure is extrapolated upstream and the strong condition is imposed upon all variables. Even for this alternative, varying free stream data may be used.

3.3.4 Pressure Outlet

Static pressure is stated at the outlet boundary where the outflow is assumed to be subsonic. However, locally supersonic outflow is also allowed, whereby outlet pressure is not specified but all variables are rather extrapolated.

3.4 The Edge Solver

3.4.1 Theoretical formulation

Edge is a parallelized flow solver able to handle unstructured two- and three-dimensional grids with elements of any shape. The equations to be solved are the compressible Reynolds-Averaged Navier-Stokes (RANS) equations, either for a steady or rotating frame of reference, but also LES or DNS (Direct Numerical Simulation) could be employed. The solver is made as an edge-based formulation and the numerical method employed is that of a node-centered, finite volume technique. The control volumes (Fig. 1) are represented by a dual grid from the control surfaces of each edge. Explicit integration of the governing equations towards steady state using the Runge-Kutta method is performed, with agglomeration multigrid and implicit residual smoothing to speed up the convergence. This convergence procedure is used as a driver of an implicit time stepping, "dual time steps", for transient analysis. Various discretization schemes are available for both the mean flow and the turbulence. Moreover, features including different gas models, steady and transient time integration and low speed preconditioning are also available. Applications within Edge include shape optimization and aero-elasticity.

3.4.2 Geometrical considerations

The preprocessor supplies a dual grid being the basis for the non-overlapping control volumes and created from the control surfaces of the edges.

The input grid in turn provides the coordinates for each node, which are connected by an edge. Additionally a control surface is provided for each edge, $\mathbf{n}S$, where $\mathbf{n}$ is the unit normal vector and S is the area. The control volume of a node is then the volume enclosed by all control surfaces of all edges emerging from that node, see Fig. 1. The surface vector for each edge is pointing away from the node of the first index and towards the node of the second index. Subsequently, the sum of all the surface vectors over a closed volume is the null vector, $\sum \mathbf{n}_i S_i = 0$, and this check is done by the preprocessor for all control

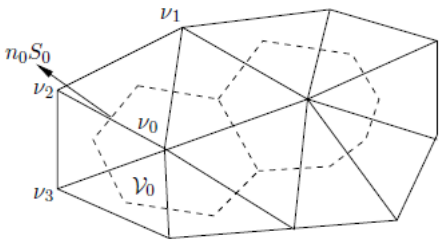

Figure 1: Edge control volume

volumes of the dual grid. Control surfaces are supplied at the boundaries so as to close the adjacent control volumes.

For a corner point, as two or more boundaries meet, the boundary control surface is split into control surfaces for each boundary condition separately. This rises the possibility of one boundary node appearing in more boundary conditions. Moreover, apart from the control surface supplied for each boundary node, an inner point is also supplied at all boundaries to be used in some of the boundary conditions. The inner node is chosen as the end node of the nearby edge closest to the boundary surface.

A similar discretization is done for 3D, where the centroid dual consists of triangular facets between the centroids of the cells, the faces and the edges. Each grid point has a control volume made up from faces intersecting the midpoint of each edge. A closed surface is formed from the faces for all edges neighbouring an internal grid point. In the case of a boundary grid point, additional boundary faces have to be added to the control volume.

3.4.3 Governing equations

The governing equations to be solved are the Navier Stokes equations, which are time-averaged to obtain the RANS equations. The time averaging is based on Boussinesq assumption and is therefore a first order closure (eqn. 2). Cartesian components are used for the flux matrices and all variables are time-averaged when the matrix systems are solved. The viscosity may either be constant or derived from Sutherland's law. Also moving and deforming grids can be handled in Edge by specifying certain parameters.

$$-\overline{\rho w_i'' w_i''} = \mu_t \left[\frac{\partial \tilde{w}_i}{\partial x_j} + \frac{\partial \tilde{w}_j}{\partial x_i} - \frac{2}{3} \left(\nabla \tilde{w} \right) \delta_{ij} \right] - \frac{2}{3} \bar{\rho} k \delta_{ij} \tag{2}$$

where w_i is the relative velocity component in the x_i-direction, μ_t is a turbulence eddy viscosity, ρ is the density and k is the turbulence kinetic energy.

Various gas models could be simulated for a calorically perfect gas, a thermally perfect gas and multiple thermally perfect gases. The calorically perfect gas is the usual assumption for aerodynamics at moderate speed. For higher temperatures, as long as no chemical reactions or ionization taking place, the assumption of a thermally perfect gas becomes more accurate. Here the variations in internal energy with temperature is due to the excitation of translational, rotational, vibrational and electronic modes of the gas molecules. The ideal gas law is still valid here, only the specific heat capacities now depending on temperature. For the mixing of thermally perfect gases, a transport equation is solved for each gas and its fraction of the total density.

3.4.4 Turbulence modeling

Three different groups of turbulence models are available in the edge formulation; RANS, DES (Detached Eddy Simulations) and hybrid LES-RANS models, as well as LES. The RANS models include a one-equation model (SA; Spalart-Allmaras model), eddy-viscosity two equation models, low Reynolds number models, EARSM:s (Explicit Algebraic Reynolds Stress Models) and differential RSM:s (Reynolds Stress Models). DES models and hybrid LES-RANS models combine a RANS model with LES and were originally developed for aeronautical applications. These include flows exhibiting unsteadiness, massive separation and vortical motions. A RANS model is used in the wall boundary layer to overcome the need for high resolution in this region as would be necessary for LES at high Re. In contrast, an LES model is used in the region outside the wall boundary layer and in regions where the flow is detached from wall surfaces. Hybrid LES-RANS models are often seen as a compromise between the computational efficiency of RANS models and the higher accuracy of LES. In Edge, the turbulence model is specified in the input file as $ITURB = 2$ for RANS, $ITURB = 3$ for DES and hybrid LES-RANS and $ITURB = 4$ for LES modeling.

Spalart-Allmaras One-Equation Model (SA) The most commonly used version of the one-equation Spalart-Allmaras model is shown here [30]. Note that the so-called "trip term" included in the original model has been dropped in the present computations, as fully turbulent flow is considered.

Therefore, also the far-field boundary condition 14 has been changed from the original publication and the new one is taken from [31, 32]

In all of the following, a "tilde" is used over the turbulence field variable. The transport equation to be solved reads as

$$\frac{\partial \tilde{\nu}}{\partial t}+u_j\frac{\partial \tilde{\nu}}{\partial x_j} = c_{b1}(1-f_{t2})\tilde{S}\tilde{\nu}-\left[c_{w1}f_w-\frac{c_{b1}}{\kappa^2}f_{t2}\right]\left(\frac{\tilde{\nu}}{d}\right)^2+\frac{1}{\sigma}\left[\frac{\partial}{\partial x_j}\left((\nu+\tilde{\nu})\frac{\partial \tilde{\nu}}{\partial x_j}\right)+c_{b2}\frac{\partial \tilde{\nu}}{\partial x_i}\frac{\partial \tilde{\nu}}{\partial x_i}\right] \tag{3}$$

and the turbulent eddy viscosity is computed from

$$\mu_t = \rho\tilde{\nu}f_{v1} \tag{4}$$

where

$$f_{v1} = \frac{\chi^3}{\chi^3+c_{v1}^3}, \quad \chi = \frac{\tilde{\nu}}{\nu} \tag{5}$$

and ρ is the density, $\nu = \mu/\rho$ is the molecular kinematic viscosity, and μ is the molecular dynamic viscosity. Additional definitions are as follows:

$$\tilde{S} = \Omega + \frac{\tilde{\nu}}{\kappa^2 d^2}f_{v2} \tag{6}$$

where $\Omega = \sqrt{2W_{ij}W_{ij}}$ is the magnitude of the vorticity, d is the distance from the field point to the nearest wall, and

$$f_{v2} = 1-\frac{\chi}{1+\chi f_{v1}}f_w = g\left[\frac{1+c_{w3}^6}{g^6+c_{w3}^6}\right]^{1/6} \tag{7}$$

$$g = r+c_{w2}(r^6-r) \tag{8}$$

$$r = \min\left[\frac{\tilde{\nu}}{\tilde{S}\kappa^2 d^2}, 10\right] \tag{9}$$

$$f_{t2} = c_{t3}\exp\left(-c_{t4}\chi^2\right) \tag{10}$$

$$W_{ij} = \frac{1}{2}\left(\frac{\partial u_i}{\partial x_j}-\frac{\partial u_j}{\partial x_i}\right) \tag{11}$$

where d is the distance to the closest surface. The constants are

$$
\begin{aligned}
\sigma &= 2/3 \\
c_{b1} &= 0.1355 \\
c_{b2} &= 0.622 \\
\kappa &= 0.41 \\
c_{w1} &= c_{b1}/\kappa^2 + (1 + c_{b2})/\sigma \\
c_{w2} &= 0.3 \\
c_{w3} &= 2 \\
c_{v1} &= 7.1 \\
c_{t3} &= 1.2 \\
c_{t4} &= 0.5
\end{aligned}
\tag{12}
$$

The boundary conditions are:

$$\tilde{\nu}_{wall} = 0 \tag{13}$$

$$\tilde{\nu}_{farfield} \in [3\nu_\infty, \quad 5\nu_\infty] \tag{14}$$

Note that $\hat{S} \geq 0$ is required in order to avoid numerical instabilities.

With the Spalart-Allmaras one-equation model, a transport equation for the turbulent viscosity is solved. This is a clear difference from earlier one-equation models, which in general solve for the turbulence kinetic energy, thereby requiring the specification of an algebraic length scale to be used with the particular flow under consideration. The model could be readily implemented on grids of any structure, which gives it an advantage over the Baldwin-Lomax and Johnson-King models.

Originally, the model was developed for high lift flows, so addressing the aerospace industry. It is calibrated on two-dimensional mixing layers, wakes and flat-plate boundary layers and has been shown to give satisfactory results for boundary layer flows in pressure gradients. In [30], two-dimensional solutions of the Navier Stokes equations including shock-induced separation and a blunt trailing edge are presented, whereby faith in the model for more complex flows is expressed. Noteworthy, for some of the cases with shock-induced separation, the model caused a pulsation of the separation bubble, whilst algebraic models generated steady solutions. Additionally, some difficulties in predicting the reattachment region in adverse pressure gradient flows are highlighted.

Similar to $k - \epsilon$ models, the SA model might suffer from an over-prediction

of the shear stresses, at least when tested on a backward facing step [30]. Anyway, the qualities of the results with the blunt trailing edge indicate that this problem cannot be very severe. Consequently, the model is believed to be most suitable for attached boundary layers and mildly separated flows [33], whereas it was shown by Wilcox [34] to be inaccurate for plane and round jets. Thus he concludes that the model is not very suitable for flows with jet-like free-shear regions. Also two-equation models such as $k-\epsilon$, $k-\omega$ and RSM (Reynolds Stress Models) are believed to be more accurate for flows involving complex recirculation and buoyancy.

Despite being primarily developed for subsonic flows around airfoils, Deck et al. [35] managed to extend the SA model to compressible supersonic flows. Thereby, they showed accurate predictions for multiple boundary layer, supersonic complex configurations with inlet flow including corners, boundary layer bleeds and struts. This is a clear development as compared to subsonic and transonic aircraft flows, that have already been successfully solved with the SA model by several other authors (e.g. [33]). A remaining challenge though is the use of the SA model for unsteady flow fields.

Hellsten $k-\omega$ model The Hellsten $k-\omega$ two-equation model was developed primarily due to the requirements of high-lift aerodynamics applications and special attention is paid to the behavior at turbulent/laminar edges, pressure gradient sensitivity and coefficient calibration. The model equations correspond to those of the Menter $k-\omega$ model (section 3.4.4) but have been completely re-calibrated, leading to improved performance over previous $k-\omega$ models. The EARSM of Wallin and Johansson [36] is used as an inherent relation between the turbulence stress tensor and the mean velocity gradient. The Hellsten model is believed to outperform most other $k-\omega$ models when it comes to the extent of applicability mainly due to the use of the EARSM model as described above and also due to the use of a wide range of flows for the coefficient calibration process. Finally, improvements over reference models were seen in a wide range of realistic test flows, especially near the edges of the turbulent regions and for flows including mild separations [17]. The transport equations for k and ω are written as [17]

$$\frac{Dk}{Dt} = P_k - \beta^* k\omega + \frac{\partial}{\partial x_k}\left[(\nu + \sigma_k \nu_T)\frac{\partial k}{\partial x_k}\right] \tag{15}$$

$$\frac{D\omega}{Dt} = \gamma \frac{\omega}{k} P_k - \beta \omega^2 + \frac{\partial}{\partial x_k}\left[(\nu + \sigma_\omega \nu_T)\frac{\partial \omega}{\partial x_k}\right] + \sigma_d \frac{1}{\omega} max(\frac{\partial k}{\partial x_k}\frac{\partial \omega}{\partial x_k}, 0) \quad (16)$$

The cross term in the ω-equation is only present when the inner product of the k and ω gradients is positive. Any of the model coefficients can be written as $C = f_{mix}C_1 + (1 - f_{mix})C_2$ where C is any of the coefficients $\gamma, \beta, \sigma_k, \sigma_\omega, \sigma_d$ and f_{mix} is a new mixing function. For more details, the reader is referred to [17]. For implementing the model in Edge, 'W&J EARSM + Hellsten k-omega' is selected among the list of RANS models.

Menter SST $k-\omega$ model The SST k-ω turbulence model [16] is a two-equation eddy-viscosity model. The SST (Shear Stress Transport) formulation combines the use of a $k-\omega$ formulation in the inner part of the boundary layer with a $k-\epsilon$ behavior in the free-stream flow field. The former feature ensures that the model is applicable all the way down to the wall, through the viscous sublayer. Therefore, the model is valid as a Low Reynolds Number model, without the necessity of including extra damping functions. In contrast, the $k-\epsilon$ formulation in the free stream diminishes the sensitivity of a normal $k-\omega$ model to the free stream turbulence. This translates into the SST $k-\omega$ model displaying good abilities in predicting adverse pressure gradients and separated flow [16]. Nonetheless, the SST $k-\omega$ overestimates the turbulence levels in regions with large normal strains, e.g. stagnation regions and those of strong acceleration. Still this effect is much smaller than for a normal $k-\epsilon$ model. The closure of the SST $k-\omega$ model is as follows [16].

Kinematic eddy viscosity

$$\nu_T = \frac{a_1 k}{\max(a_1 \omega, SF_2)} \quad (17)$$

Turbulence kinetic energy

$$\frac{\partial k}{\partial t} + U_j \frac{\partial k}{\partial x_j} = P_k - \beta^* k\omega + \frac{\partial}{\partial x_j}\left[(\nu + \sigma_k \nu_T)\frac{\partial k}{\partial x_j}\right] \quad (18)$$

Specific dissipation rate

$$\frac{\partial \omega}{\partial t} + U_j \frac{\partial \omega}{\partial x_j} = \alpha S^2 - \beta \omega^2 + \frac{\partial}{\partial x_j}\left[(\nu + \sigma_\omega \nu_T)\frac{\partial \omega}{\partial x_j}\right] + 2(1 - F_1)\sigma_{\omega 2}\frac{1}{\omega}\frac{\partial k}{\partial x_i}\frac{\partial \omega}{\partial x_i} \tag{19}$$

Closure coefficients and auxiliary relations

$$F_2 = \tanh\left[\left[\max\left(\frac{2\sqrt{k}}{\beta^* \omega y}, \frac{500\nu}{y^2 \omega}\right)\right]^2\right] \tag{20}$$

$$P_k = \tau_{ij}\frac{\partial U_i}{\partial x_j} \tag{21}$$

$$F_1 = \tanh\left\{\left\{\min\left[\max\left(\frac{\sqrt{k}}{\beta^* \omega y}, \frac{500\nu}{y^2 \omega}\right), \frac{4\sigma_{\omega 2} k}{CD_{k\omega} y^2}\right]\right\}^4\right\} \tag{22}$$

$$CD_{k\omega} = \max\left(2\rho\sigma_{\omega 2}\frac{1}{\omega}\frac{\partial k}{\partial x_i}\frac{\partial \omega}{\partial x_i}, 10^{-10}\right) \tag{23}$$

$$\phi = \phi_1 F_1 + \phi_2(1 - F_1) \tag{24}$$

$$\alpha_1 = \frac{5}{9}, \alpha_2 = 0.44 \tag{25}$$

$$\beta_1 = \frac{3}{40}, \beta_2 = 0.0828 \tag{26}$$

$$\beta^* = \frac{9}{100} \tag{27}$$

$$\sigma_{k1} = 0.85, \sigma_{k2} = 1 \tag{28}$$

$$\sigma_{\omega 1} = 0.5, \sigma_{\omega 2} = 0.856 \tag{29}$$

For using the SST Menter $k - \omega$ model in Edge, 'Menter SST k-omega' is selected among the available RANS models.

The SST model was developed for predicting aeronautics flows with strong adverse pressure gradients and separation. This has been partly motivated by the failure of turbulence models commonly used in previous aeronautic appli-

cations, for which the conventional linear $k-\epsilon$ model often fails to represent turbulent boundary-layer separation and the Johnson-King model may become awkward to extend to three-dimentional computations due to its algebraic formulation. Additionally, $k-\omega$ models, despite being more accurate than $k-\epsilon$ models in the near wall layers, fails for flows with pressure induced separation and are thus only applicable to flows with a moderately adverse pressure gradient.

A major weakness of the SST $k-\omega$ model is its dependence on the value of ω in the free stream, i.e. outside the boundary layer, which is the major reason preventing it from replacing the ϵ-equation as the standard in turbulence modeling. However, due to its near-wall superiority, there is a huge motivation for developing improved $k-\omega$ models but also so called zonal baseline (BSL) models. The latter is similar to the original Wilcox $k-\omega$ model [37], but has overcome the strong dependency on free stream values [16]. This is accomplished by employing a blend of $k-\epsilon$ and $k-w$ models for different regions of the flow and thus requires wall distances, which are obtained by solving the Poisson equation.

What has made the SST formulation so successful is the influence from previous turbulence models, especially the near-wall formulation of the Wilcox standard $k-\omega$ model (section 3.4.4). Apart from small areas of improvements, the original SST model is used for most purposes. Areas where improvements are eligible include robustness so as to get the same rate of convergence as $k-\epsilon$ formulations with wall functions, as well as improved near-wall formulations, reducing the grid resolution required close to the wall.

In general, RANS models under-predict the level of the Reynolds stresses in the detached shear layer emanating from a separation line [14] and thus cannot accurately predict the flow recovery downstream of the re-attachment region. In contrast, the SA and SST models have been shown to over-predict the extent of the separated region in the 9:th ERCOFTAC/IAHR/COST Workshop on Refined Turbulence Modeling for the flow over a periodic hill [13]. In an axi-symmetric diffuser test [15] the SST model has been shown to predict separation better than $k-\epsilon$ models but recovery worse, as compared to experimental data. This is reasonable as an under-prediction of the separation should allow for a better prediction of the recovery region.

Wilcox standard $k-\omega$ model The closure for the Wilcox standard $k-\omega$ model , is as follows [37].

Kinematic eddy viscosity:

$$\nu_T = \frac{k}{\omega} \tag{30}$$

Turbulence kinetic energy:

$$\frac{\partial k}{\partial t} + U_j \frac{\partial k}{\partial x_j} = \tau_{ij} \frac{\partial U_i}{\partial x_j} - \beta^* k\omega + \frac{\partial}{\partial x_j} \left[(\nu + \sigma^* \nu_T) \frac{\partial k}{\partial x_j} \right] \tag{31}$$

Specific dissipation rate:

$$\frac{\partial \omega}{\partial t} + U_j \frac{\partial \omega}{\partial x_j} = \alpha \frac{\omega}{k} \tau_{ij} \frac{\partial U_i}{\partial x_j} - \beta \omega^2 + \frac{\partial}{\partial x_j} \left[(\nu + \sigma \nu_T) \frac{\partial \omega}{\partial x_j} \right] \tag{32}$$

Closure coefficients and auxiliary relations: $\alpha = \frac{5}{9}$, $\beta = \frac{3}{40}$, $\beta^* = \frac{9}{100}$, $\sigma = \frac{1}{2}$, $\sigma^* = \frac{1}{2}$ and $\varepsilon = \beta^* \omega k$.

One of the major problems with the Wilcox standard model is its dependency on free-stream quantities, which is a reason for the development of the SST model as discussed above. To use it in Edge, 'std Wilcox k-omega' is selected.

The Peng-Davidson-Holmberg (PDH) LRN $k-\omega$ model The PDH Low Reynolds Number (LRN) model [12] is based on the $k-\omega$ model with damping functions to deal with near-wall viscous effects. The model was orignally developed for internal turbulent flows with flow separation, recirculation and reattachment.

The PDH model is a low Reynolds number model based on Wilcox two-equation LRN $k-\omega$ formulation [10]. The major motivation for the modified model is a better prediction of internal recirculating flows. Moreover, the original model under-predicts the turbulence kinetic energy close to the wall, whereas the modified version has proved a correct near-wall behavior due to the cross-diffusion term. Additionally, this term does not seem to affect the turbulent length scale in the vicinity of the reattachment zone, as compared to low Re $k-\epsilon$ models heavily over-predicting it. Still the cross-diffusion term manages to eliminate the freestream dependence of ω, which is a limitation of the original model. During evaluation, the PDH model has described the near wall low Re effect for attached turbulent channel flows but further evaluation is needed for adverse pressure gradient boundary layer flows. For separated and recirculating flows, the model has shown to balance the damping of the near-wall turbulence and the enhancement of the near-wall turbulence kinetic energy, which is underpredicted by the Wilcox original model. The modified ω-equation, the damping

functions and the model constants read as follows.

$$\frac{D(\rho\omega)}{Dt}+\frac{\partial(\rho u_j\omega)}{\partial x_j}=c_{\omega1}f_\omega\frac{\omega}{k}P_k-c_{\omega2}\rho\omega^2+\frac{\partial}{\partial x_j}\left[\left(\mu+\frac{\mu_t}{\sigma_\omega}\right)\frac{\partial\omega}{\partial x_j}\right]+c_\omega\frac{\mu_t}{k}\left(\frac{\partial k}{\partial x_j}\frac{\partial\omega}{\partial x_j}\right) \tag{33}$$

$$P_k=-\rho\overline{u_i'u_j'}\frac{\partial u_i}{\partial x_j}=\mu_t\left(\frac{\partial u_i}{\partial x_j}+\frac{\partial u_j}{\partial x_i}\right)\frac{\partial u_i}{\partial x_j} \tag{34}$$

$$c_\mu=1.0,\quad c_k=0.09,\quad c_{\omega1}=0.42,\quad c_{\omega2}=0.075,\quad c_\omega=0.75,\quad \sigma_k=0.8\quad and\quad \sigma_\omega=1.35$$

$$f_\mu=0.025+\left\{1-exp\left[-\left(\frac{R_t}{10}\right)^{3/4}\right]\right\}\times\left\{0.975+\frac{0.001}{R_t}exp\left[-\left(\frac{R_t}{200}\right)^2\right]\right\} \tag{35}$$

$$f_k=1-0.722exp\left[-\left(\frac{R_t}{10}\right)^4\right] \tag{36}$$

$$f_\omega=1+4.3exp\left[-\left(\frac{R_t}{1.5}\right)^{1/2}\right] \tag{37}$$

where R_t is the turbulent Reynolds number.

To use the model in Edge, 'PDH LRN k-omega' is set as the turbulence model.

3.4.5 Running Edge

Initially, the preprocessor has to be run to generate the **.bedg**-files containing information about the edges and control volumes of the grid nodes, as well as partitions for computations using multiple processors. The input arguments for the preprocessor, solver and post-processor are defined and supplied by an input file, **.ainp**. Here fluid properties, numerical parameters, turbulence modeling, transient settings etc are specified. Secondly, the boundary conditions are implemented and saved in the **.aboc**-file, again using the input-file **.ainp**. Paths to the **.bedg-**, **.bmsh-**, and **.aboc**-files are specified in the input file.

Once the preprocessor has been run and the boundary conditions specified, the flow solver could be run by submitting the input file. For this investiga-

tion, the Beda-cluster was used for parallel computations with 4 CPU:s each comprising 4 cores for a total of 16 cores. In post-processing the results, the solution files **.bout** were merged using the command **merge_partitions** and information extracted from the resulting single **.bout**-file using the command **ffa2engold**. Thus information on flow field properties was generated and the file **.case** could be loaded into the post-processing tool **Ensight** for flow field analysis.

When running Edge, a residual file, **.bres**, is generated with the residuals for the density, velocity components, total energy, turbulence kinetic energy and a turbulence property, such as ω for $k-\omega$ models, but also integrated forces and moments. This file could subsequently be used so as to assess the level of convergence of the solution.

A simulation could be started from scratch but also from an initial solution by specifying **.bini** initial files, or as a continuation of a previous run by giving the previous output-file **.bout** as an input. This is specified thorough the parameter $INPRES$ in the **.ainp**-file. For more information about the different parameters and file types used with Edge, the reader is referred to the Edge documentation [38].

4 Methodology

4.1 Grid

The experimental setup for obtaining data to evaluate the numerical results against is shown in Fig. 2. The shock is held at the center line of the viewing window by controlling the settling chamber pressure. The top and bottom parts of the convergent-divergent nozzle could be changed so as to obtain the different Mach numbers 1.3, 1.4 and 1.5, which are all obtained $30mm$ upstream of the shock position by means of tunnel floor static pressure measurements. The walls of the wind tunnel are solid and it exhausts into the atmosphere. In Table 1 the dimensions of the test section are displayed.

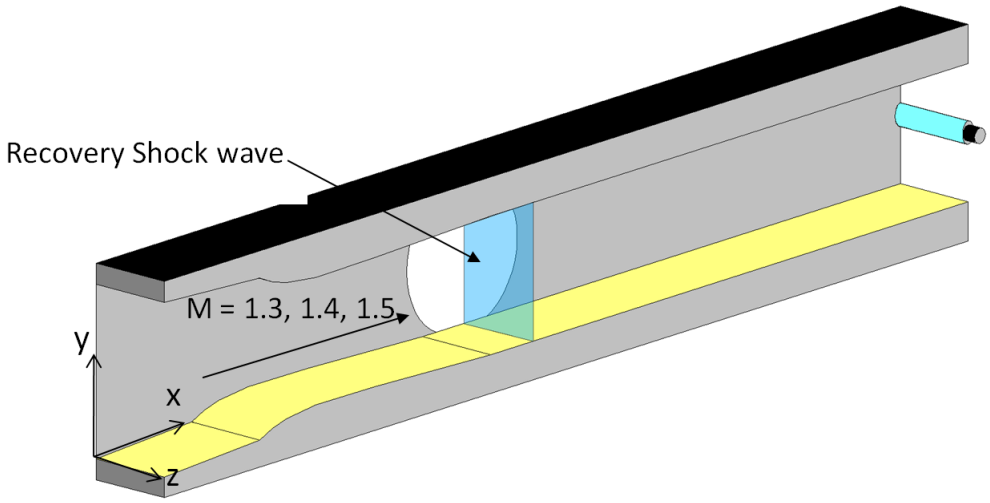

Figure 2: Experimental wind tunnel set-up

Test section height [mm]	178
Test section width [mm]	114
Distance from nozzle throat to shock [mm]	516

Table 1: Wind tunnel dimensions for experimental set-up

Mach	N_x	N_y	N_z	File format
1.3	265 nodes	129 nodes	97 nodes	structured cgns
1.4	265 nodes	129 nodes	97 nodes	structured cgns

Table 2: Grid specifications for Mach 1.3 and 1.4

4.2 Running the case in Edge

4.2.1 Edge files

The **.ainp** defines the turbulence model to be used, e.g., the Hellsten, SA and SST models for $M = 1.3$ and the PDH and Wilcox models for $M = 1.4$. The

preprocessor reads this input-file and generates **.bedg-** files. Usually, in spite of different models being selected in different runs for the same flow problem, the same **.bedg**-file can be used, since this file consists only of information related to geometries. It should be noted, however, that different **.bedg**-files may need to be re-generated due to different modelling formulations. For example, the **.bedg**-files generated for a $k-\omega$ model that does not invoke wall distance, cannot be used by another model in which the wall distance is required. In the present computations, the same **.bedg**-files were used for the Hellsten and the SST models, whilst new ones were generated for the SA model. Similarly, the Wilcox model and the PDH model share a common set of **.bedg**-files, as both models are based on similar $k-\omega$ formulations.

Boundary conditions were specified when running the program **bound** as follows. The total states inlet condition (number 34) for the inflow boundary, pressure outlet (number 37) for the outlet boundary, and adiabatic wall (number 12) for the top, bottom and side wall boundaries. For the walls, a strong or weak formulation is selected after specifying the boundary type by choosing to set additional parameters as asked for from the application bound. Similarly, no wall functions are specified but this could be done if required. Total states are defined at the inlet, i.e. temperature and pressure, and the back pressure is defined at the outlet. The back pressure is the independent variable to be altered in order to make the shock location change. However, the relationship is revealed in an empirical manner, as no simple relation exists. The settings of the **.aboc**-file could be changed even after running **bound**; simply by opening the **.aboc**-file in a text editor and modify it as required. This is the case also for the **.ainp**-file but not for the **.bmsh-** and **.bedg**-files.

Important to mention here is that due to a continuous update of the Edge software, several different versions exist. Anyhow, the file types required by Edge are not compatible between the different versions and therefore care must be taken and the preprocessor and **bound** have to be run again when switching between versions, and the correct version of the **.ainp**-file has to be used. The differences between the different versions are small but yet significant ones. For example, the coefficient for calculating ω_0, i.e. ω at the wall boundary node, has been changed from 1.5 for some $k-\omega$ models in Edge version 4.1 (referred to as the "old" version) to 10 in version 5.0 (referred to as the "new" version). Consequently, slight differences may be observed in the solutions obtained with $k-\omega$ models, when switching between the versions.

After the simulation, an output file, **.bout**, or one for each partition if Edge

is run in parallel, is created. This file can be converted to post-processing format with the **ffa2engold** command. Thus common fluid parameters are extracted for post-processing with the tool **Ensight**. If additional parameters are required, this can be specified in the **.ainp**-file. However, for the present analysis, the standard information as obtained from Edge has been considered.

4.2.2 Edge parameters

In the **.ainp**-file, the default parameters have been used as extensively as possible, as the intention has been to evaluate how reasonable these settings are. However, some modifications depending on the flow case at hand have been inevitable. In order to adjust for numerical stability issues, a CFL number in the range $[0.25, 1.25]$ has been used with the lower limit for more sensitive cases. Moreover, the CFL number has sometimes been increased once recognizing the solver display a stable process. In order to speed up convergence, a high CFL number is to prefer, as is the use of multigrid levels. Four multigrid levels have been used except for the PDH model, where the number has been reduced to three due to divergence problems.

4.2.3 Numerical scheme

For all cases, the second-order central differencing scheme has been used for the momentum equations. A second-order upwind scheme has been used for the turbulent transport equations, which in Edge is available as a bounded scheme, similar to the van Leer scheme. Using a second-order bounded upwind scheme is sometimes considered superior to the central scheme, as this takes into account the flow direction and is often numerically more stable. Nevertheless, the second-order upwind scheme may become too diffusive and may smear the resolution of the shock wave and neglect interesting local flow features. The central scheme, on the other hand, imposes usually less artificial dissipation and may thus give a better resolution of the flow field. Note that the central scheme is unbounded and numerically more unstable, as compared to upwind schemes. For this investigation the convergence of the solution has been speeded up by using a full multigrid approach and implicit residual smoothing.

4.3 Streamwise shock location vs. back pressure and convergence level

In order to compare the simulated pressure and velocity profiles to the experimental data available [20], the simulated shock position must be in agreement with the experimental one. Thus the back-pressure at the outlet of the duct was adjusted, so as to make the shock position fit the experimental results as close as possible. In the experiment, the back pressure was not measured at the outflow section, as being specified in the computational domain. A discrepancy in shock position of maximum $7mm$ has been accepted as reasonable in comprising only about 1.22% of the total length of the bump. As an initial conjecture, the back pressure for numerical studies as indicated in the ATAAC test-case description [20], was used for each respective Mach number and type of turbulence model; as far as such guidelines were available. In cases where simulation data from previous investigations of a particular turbulence model were absent, a sophisticated guess based on scientific reviews served as a starting point. Worth mentioning here is that the shock position by no means displayed a linear behavior with regard to the back pressure, thus making the adjustment procedure much of a trial and error process with huge variety in shock displacement due to a certain leap in back pressure. Therefore, an initial attempt at interpolating the correct back pressure from simulations with different back pressures for a certain turbulence model was quickly abandoned with the adjustment thus being more based on intuition and previous experience.

Furthermore, the shock position was very sensitive to back pressure variations, requiring very small changes in back pressure to be taken each time to find the correct one. In addition, the simulations had to be sufficiently converged in order to give a reliable shock position; in this case the convergence of primarily the integrated drag force was required as well as converged residuals. For the integrated lift force and momentum, these are of less importance for internal duct flow. Also, the position of the shock for a certain setup should ultimately stay constant as the simulation was run further in order to yield a steady state solution. This proves to be an important criterion as the shock position might change substantially for a constant back pressure as the convergence of the solution is driven down as is obvious from Fig. 6, 7, 8, 9 and 10.

For $M = 1.3$, three different RANS turbulence models were evaluated; those being the Hellsten $k-\omega$ model, the SA model and the Menter SST $k-\omega$ model.

As prediction abilities vary greatly for the different models, initial as well as adjusted back pressure is unique to each model. For each simulation setting, default parameters in the Edge input-file were retained as far as possible. Major alterations were confined to the CFL number in order to keep the calculations numerically stable.

For $M = 1.4$, four RANS turbulence models were initially investigated; the Menter SST $k - \omega$ model, the SA model, the Wilcox standard $k - \omega$ model and the PDH model. As an initial conjecture of the correct back pressure, the outlet pressure as specified [20] was used for the SA model and a somewhat higher pressure for the other four models. However, the former two models displayed very asymmetric predictions of boundary layer separation, as well as two consecutive shock waves. Thus the problem of where to define the shock position for their respective solutions rendered further investigation farcical, as is clear from Fig. 5. In contrast, the Wilcox and PDH models resulted in very clear and consistent predictions of the shock position, see Fig. 4. Consequently, the same procedure for finding the shock position corresponding to the experimental values as for $M = 1.3$, was performed for these two models.

When estimating the position of the shock from the numerical results, a C_P profile was plotted along the geometrical center line of the duct geometry using the visualization software **Ensight**. The shock position was then defined as the horizontal point where the C_P value reached a maximum, i.e. just before the C_P profile attaining a negative slope as indicated in Fig. 6 to 10. For a comparison, a solid line is representing the x-coordinate corresponding to the experimental value for the shock position.

In order to investigate eventual asymmetry of the velocity field, streamlines and Mach surfaces (Fig. 23 for $M = 1.3$ and Fig. 24 for $M = 1.4$) are drawn of cross-sections of the duct at the position of the shock. Another feature of the experimental data available is the values for Mach number being based on measurements of tunnel floor static pressure at $30mm$ upstream of the shock location. Thus, ideally, the simulations should yield the correct Mach number at exactly this position in the duct. At this very initial stage though, the proper positioning of the shock is considered as more important than that of the Mach number measurement point.

4.4 Boundary conditions

For all models, strong adiabatic boundary conditions were used for the top, bottom and side walls, corresponding to number 12 in the Edge boundary conditions list. Velocity inlet (number 34) were used for the inflow boundary and pressure outlet (number 37) for the outlet boundary. The reason for using strong rather than weak wall boundary conditions was due to an initial observation that weak boundary conditions might generate an unphysical delay of the streamwise shock position. Also strong boundary conditions are physically more accurate (section 3.3). Such an approach normally works well where no major convergence problems are experienced.

A comparison of the effect of weak versus strong wall boundary conditions was performed as part of the evaluation for the Hellsten model at $M = 1.3$ and a back pressure of $115800Pa$. Once a converged solution with the correct position of the shock was obtained using strong boundary conditions, with the same settings, the computation is re-run using the weak wall boundary condition. The results were then compared to those with strong boundary conditions to reveal the changes of the flow field, shock movement etc.

4.5 Separation of flow

In order to investigate the prediction of separation for the different models tested, skin-friction patterns along the top, bottom and side walls, as well as an x-wise cross-section of the duct, are plotted. The separation bubbles detected have been measured using **Ensight**. The main reason for doing this is to investigate the position of interaction between the shock wave and the boundary layer, and the size of the separation bubbles, as well as the symmetry of the flow. It is noted that the flow features at the $x - y$ mid-section have also been highlighted, in order to demonstrate the location of shock wave.

5 Results

5.1 Shock position versus back pressure

As mentioned, the experimentally measured pressure is not available at the outflow section of the computational domain. In order to get the computed shock position in consistence with the experimental observation, the back pressure at the duct outlet has been adjusted in the simulations with different turbulence

models. Consequently, by adjusting the back pressure at the duct outflow section, simulations for all models presented here generated the shock wave at a position in satisfying agreement with the shock position from the experimental data. In Table 3, the shock position for each model can be seen, together with its deviation from the experimental value. The streamwise location of the shock for each model has been estimated by plotting the pressure coefficient along the geometrical center-line in the stream wise direction. The position of the shock is then taken as the point where C_P reaches a maximum, i.e. before its derivative turns negative. Altogether, about 40 different back pressures were tested for the three models at $M = 1.3$ and about 20 for the two models at $M = 1.4$. Also the SA and SST models were tested at $M = 1.4$. The results show that the two models fail to produce a distinguishable shock wave (see Fig. 5), where the shock-induced boundary layer separation is exaggerated and the shock becomes rather smeared. These results are thus not included in this report.

Mach-number contours for the three models tested with $M = 1.3$ are displayed in Fig. 3. It can be seen that the SA and SST models are subject to vague compression regions slightly downstream of the main shock position, whereas for the Hellsten model, only one distinct shock appears.

Turbulence model	Hellsten	SA	SST	PDH	Wilcox	Experiment
Mach number	1.3	1.3	1.3	1.4	1.4	1.3 and 1.4
Back pressure [Pa]	115800	113000	114400	83500	87000	-
x-coordinate shock position [m]	0.664	0.654	0.659	0.663	0.666	0.659
Deviation [mm]	+5	-5	0	+4	+7	-
% deviation	0.87	0.87	0	0.70	1.22	-

Table 3: Numerical prediction of shock position for investigated turbulence models

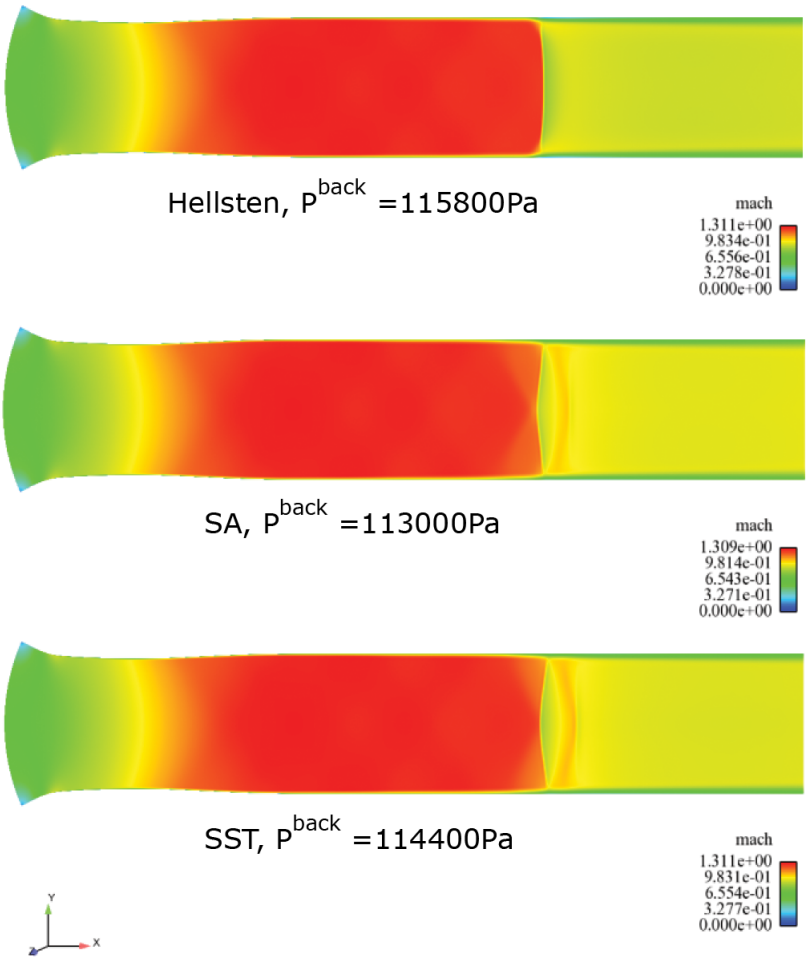

Figure 3: Contours of the Mach number computed by different models at $M = 1.3$. The Hellsten EARSM $k-\omega$ model (top), the SA model (middle) and the SST model (bottom). Different back pressures have also been given in the figure. $M = 1.3$ is referred to the Mach number measured at $30mm$ upstream of the shock location. Side view of center plane.

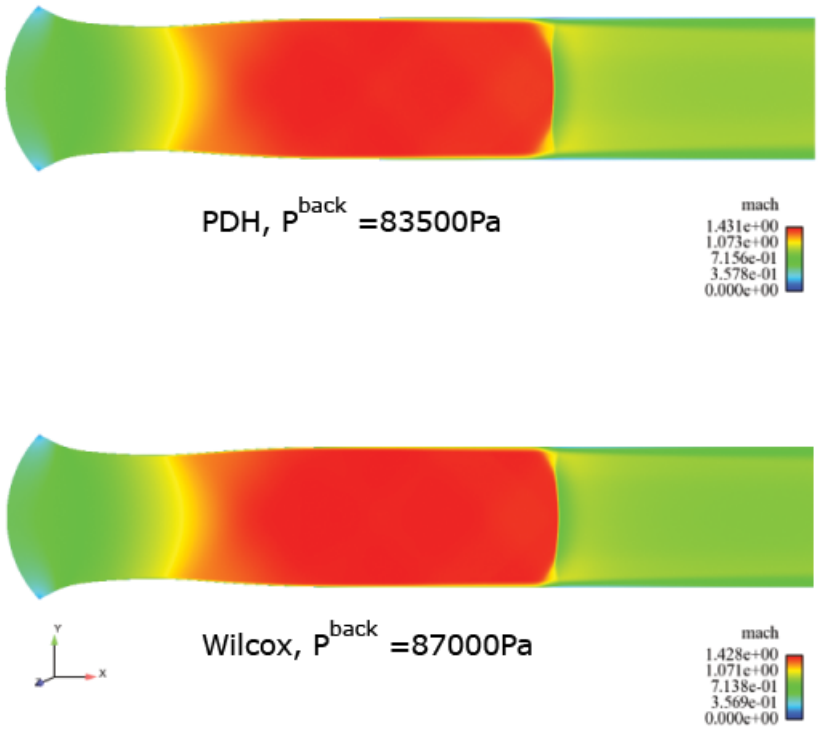

Figure 4: Contours of the Mach number computed by different models at $M = 1.4$. The PDH model (top) and the Wilcox model (bottom). Different back pressures have also been given in the figure. $M = 1.4$ is referred to the Mach number measured at $30mm$ upstream of the shock location. Side view of center plane.

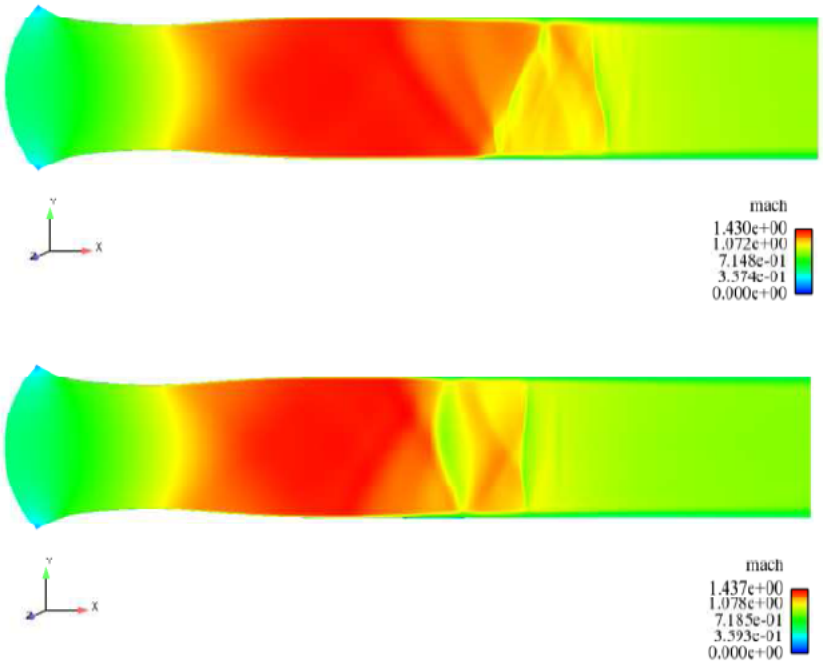

Figure 5: Contours of the Mach number computed by different models at $M = 1.4$. The SA model (top), $P^{back} = 83780Pa$, and the SST model (bottom), $P^{back} = 85500Pa$. $M = 1.4$ is referred to the Mach number measured at $30mm$ upstream of the shock location. Side view of center plane.

In a similar manner, the Mach surfaces are shown for the final results of $M = 1.4$ in Fig. 4. Apparently, both models have predicted a distinct shock wave. In contrast, the computed shock wave is smeared at $M = 1.4$ with the SA and SST models (see Fig. 5).

5.2 Effect of solution convergence on shock position

5.2.1 Hellsten, SA and SST model for Mach 1.3

The movement of the shock with respect to the level of convergence, for fixed back pressure at $M = 1.3$, is illustrated in Fig. 6 to 8 for some selected cases, for which the convergence has been intentionally driven down, including the final results. The maximum level of convergence for the density, the velocity components, the total energy, the turbulence kinetic energy (k) and the turbulent eddy viscosity ($\tilde{\nu}$) for the SA model or the specific dissipation rate (ω) for the

$k-\omega$ model, is given in the illustration legend together with the back pressure specied for each particular computation.

As shown in Fig. 6, the results obtained with the SA model indicate that, when the residual has been reduced down to a certain order of magnitude, say, $1e-8$ or $1e-5$ for a back pressure of $112100Pa$ or $113000Pa$, respectively, the solution, as far as the position of the shock is concerned, is no more sensitive to further residual reduction.

For the SST model, sufficient convergence for shock steadiness is obtained only for a back pressure of $115100Pa$ at a level of about $1e-2$ (see Fig. 7). For the other back pressures used with the SST model, small but significant shifts of the shock are observed. A relatively large variation in the computed shock location is observed for the poorly converged solution with back pressure $115000Pa$. These results can be seen in Fig. 7, where the back pressure together with the level of convergence is indicated for each solution. Comparing the patterns of shock movement for the SST model with back pressure $114400Pa$, which is the solution used for further analysis, to those obtained for back pressure $115100Pa$, similarities are seen and therefore faith is held in the $114400Pa$ solution being sufficiently converged.

For the Hellsten model, it can be seen that the shock is shifted downstream as the level of convergence improves, with the greatest leap in shock position occurring for successive convergence levels at a back pressure of $115600Pa$, as displayed in Fig. 8.

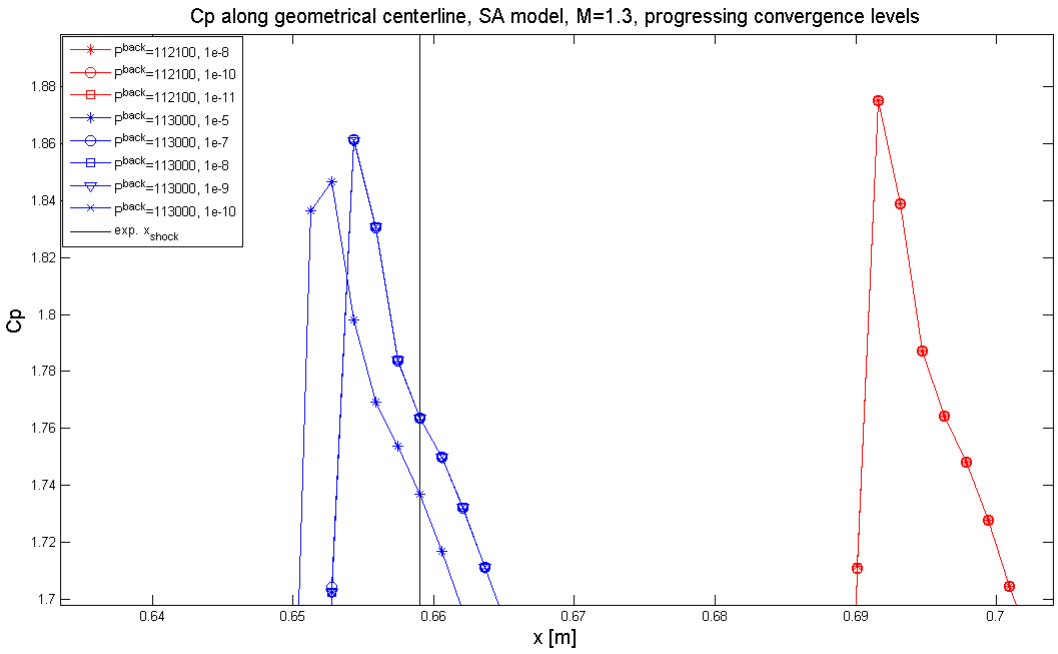

Figure 6: C_P along geometrical center line, SA model, successive convergence levels, $M = 1.3$

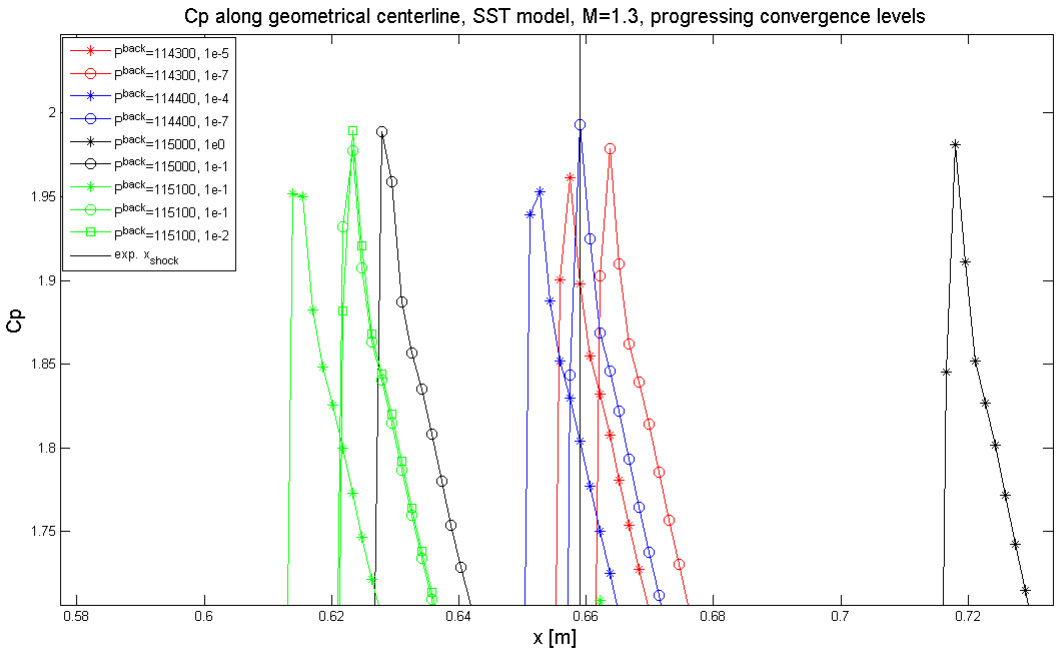

Figure 7: C_P along geometrical center line, SST model, successive convergence levels, $M = 1.3$

5.2.2 PDH and Wilcox model for Mach 1.4

For the PDH model, the best results regarding shock position are obtained for a back pressure of $83500Pa$, with a convergence level of approximately $1e-4$. For two successive runs, the shock can be seen to move only slightly (black lines, * and o label).

With the Wilcox model, a reliable degree of convergence, here $1e-3$, is obtained only for back pressure $86900Pa$ (black lines, Fig. 10), where the two last successive solutions produce pressure coefficient distributions collapsing upon each other (black lines, square and v label) as seen in Fig. 10. However, the results used as final are those with back pressure $87000Pa$ (green lines, Fig. 10), and since the behavior of successive solutions for this case is similar to that with back pressure $86900Pa$ (black lines, Fig. 10), the results are assumed to be fairly converged. It should be noted that further simulations with back pressure $87000Pa$ were not possible due to limited computer resources.

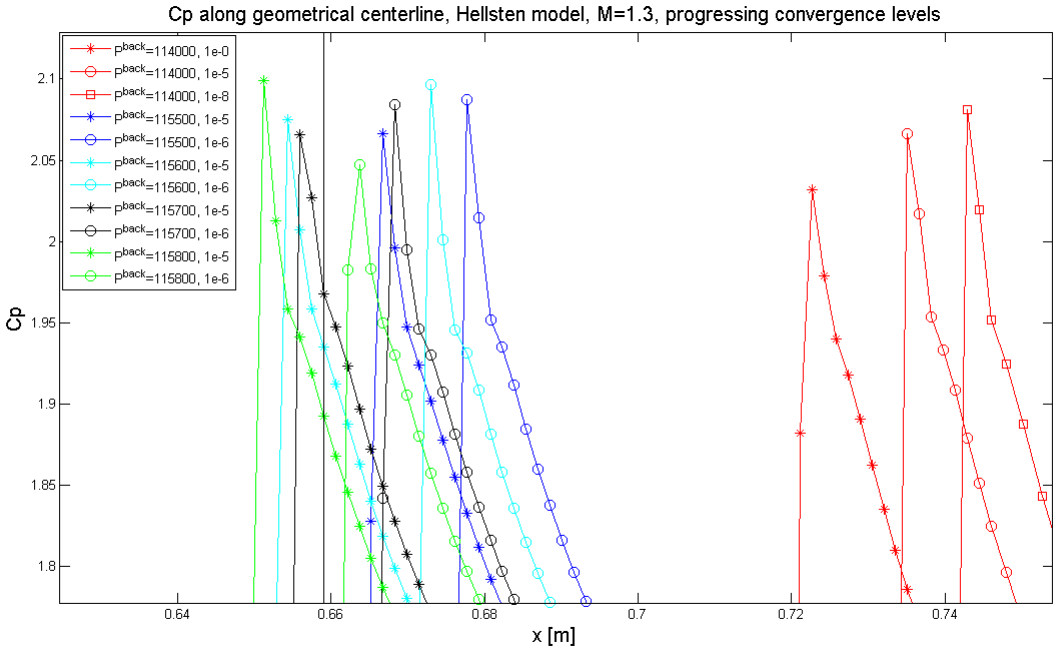

Figure 8: C_P along geometrical center line, Hellsten model, successive convergence levels, $M = 1.3$

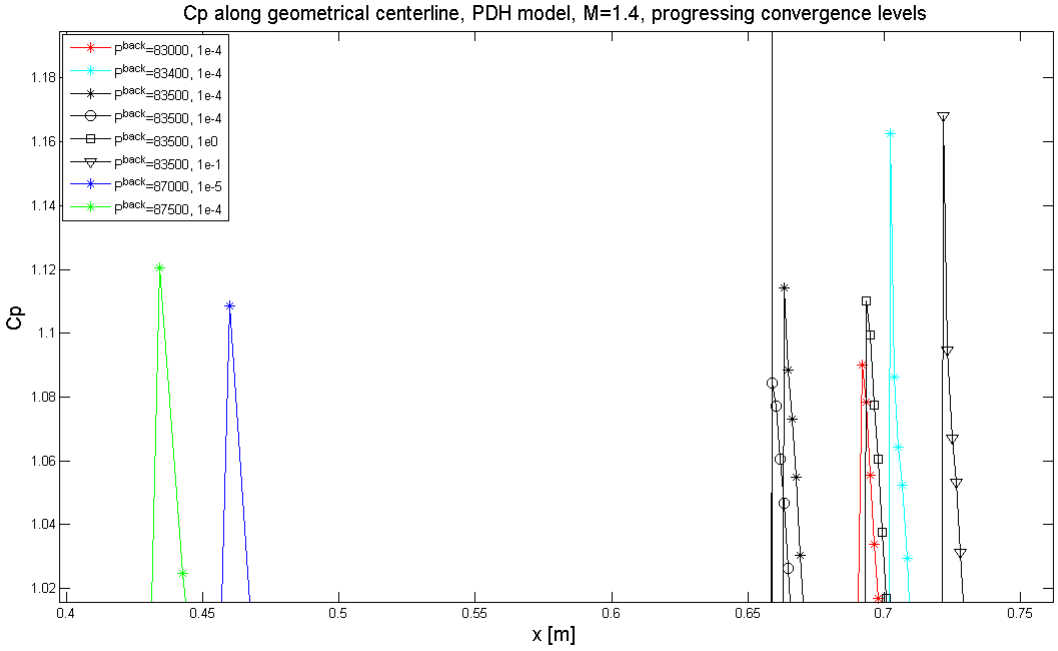

Figure 9: C_P along geometrical center line, PDH model, successive convergence levels, $M = 1.4$

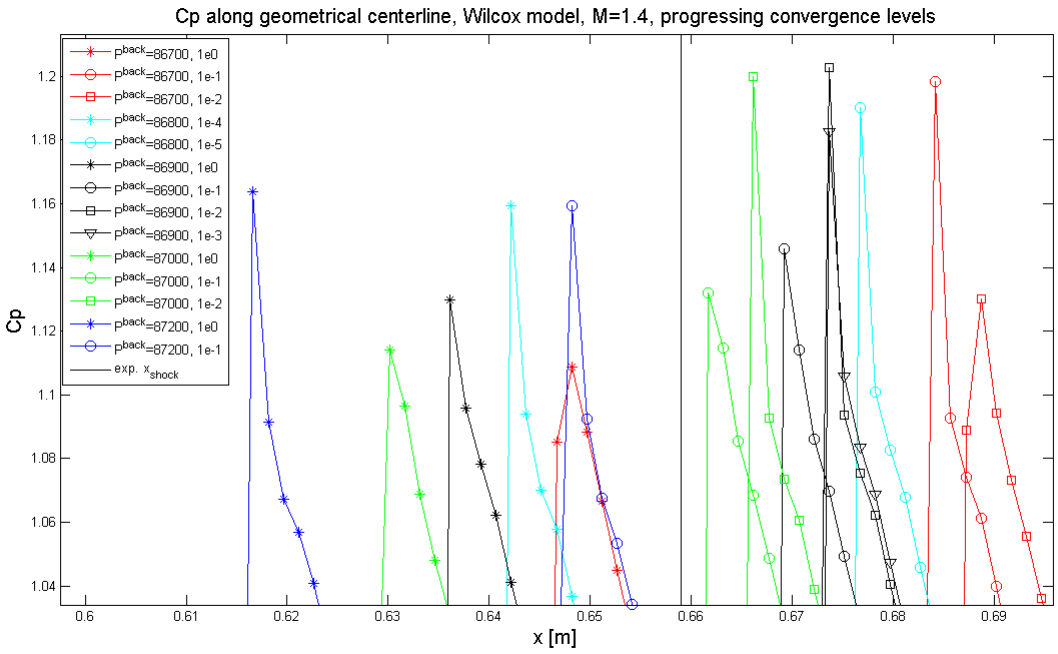

Figure 10: C_P along geometrical center line, Wilcox model, successive convergence levels, $M = 1.4$

5.2.3 Comments

It is obvious that the residuals have to be driven down to a sufficiently low level in order to get converged solution. This is particularly true for the predicted shock location, which is very sensitive to the convergence. However, the shifting of the shock wave during the solution convergence is seemingly not monotonic, but is moving back and forth with decreasing residuals. The solution convergence is related to the turbulence model and the back pressure specified, and certainly to a wide range of other parameters, the impact of which has not been assessed here. More investigation is thus needed in order to explore the effect of solution convergence on the prediction of SWBLI:s using the Edge software.

5.3 Velocity Profiles

Experimental data on velocity profiles are available for streamwise positions from the inlet to the position of the shock and within the region of SWTBLI. Reference points used are those from the available experimental data, with $x = 0$

at the position of the shock and $y = 0$ at the bottom wall of the duct. Note that the reference point for each numerical solution is that of the shock prediction for that particular case, since the exact position of the shock at $659mm$ downstream was very hard to obtain. For the numerical results of Table 3, velocity profiles have been extracted at streamwise positions corresponding to those for which experimental data are available, using the position of the shock as a reference point for each case rather than the x-coordinate of the inlet boundary. This means that the computed velocity profile, compared to the experimental data measured at $30mm$ upstream of the experimental shock position at $x = 659mm$, will be taken at $30mm$ upstream of the predicted shock position (thus not necessarily at $x = 629mm$). Experimental velocity profiles are available at

$$x = [-250,\ -200,\ -150,\ -100,\ -500,\ +50,\ +100,\ +150,\ +200,\ +250]mm$$

for both $M = 1.3$ and $M = 1.4$

Interaction velocity profiles are available for

$$x = [-32,\ -22,\ -17,\ -13,\ -7,\ -4,\ -20,\ +2,\ +5,\ +10,\ +15,\ +20,\ +30]mm$$

for $M = 1.3$ and

$$x = [-30,\ -20,\ -15,\ -10,\ -5,\ -20,\ +2,\ +5,\ +10,\ +15,\ +20,\ +30]mm$$

for $M = 1.4$

For $M = 1.3$, a trend can be seen for the numerical interaction velocity profiles when it comes to the agreement with the experimental data available. Far upstream in the interaction region, i.e. for $x \in [-32, -17]mm$, the velocity profile for the Hellsten model is closer to the experimental ones than those for the SA and SST models as can be seen in Fig. 11 for $x = -32mm$. Approaching the shock, the SA and SST subsequently improves over the Hellsten model, especially close to the wall as can be observed in Fig. 12 for $x = -13mm$. Nevertheless, at this point, the Hellsten model has produced the velocity profile in better agreement with the experimental data, partiucularly in the central part of the duct. In contrast, within the intermediate proximity of the shock, including the position of the shock itself, the SA and SST model correspond more closely to the experimental velocity profiles as can be seen in Fig. 13 of the velocity profiles at the shock position. This tendency is observed for streamwise

positions of $x \in [-13, +2]mm$, with raising ambiguity with increasing distance from the shock. For example, the case for $x = +5mm$ in Fig. 14 shows a better agreement with experimental results for the SA and SST models when it comes to the shape of the profile, whereas the Hellsten model seem to better correspond to the magnitude of the experimental data. Downstream of the shock location, the SA and SST velocity profiles are observed to collapse fairly well onto the experimental one, whereas the Hellsten profile is closer in magnitude to the experimental data. At $x = +40mm$, the Hellsten velocity profile agree well to the experimental one very close to the wall, with the SA and SST models better reflecting it for a very short distance a bit further from the wall, and then the Hellsten model again better describing experimental data at the last part of its profile. This is highlighted in Fig. 15.

The results shown in Fig. 11 and 12 indicate that the SA, SST and Hellsten models have in general over-predicted the boundary layer thickness, when approaching the shock location. Downstream of the shock location, as shown in Fig. 14 and 15, the predicted velocity profiles in the near-wall boundary layer are in reasonable agreement with the experiments.

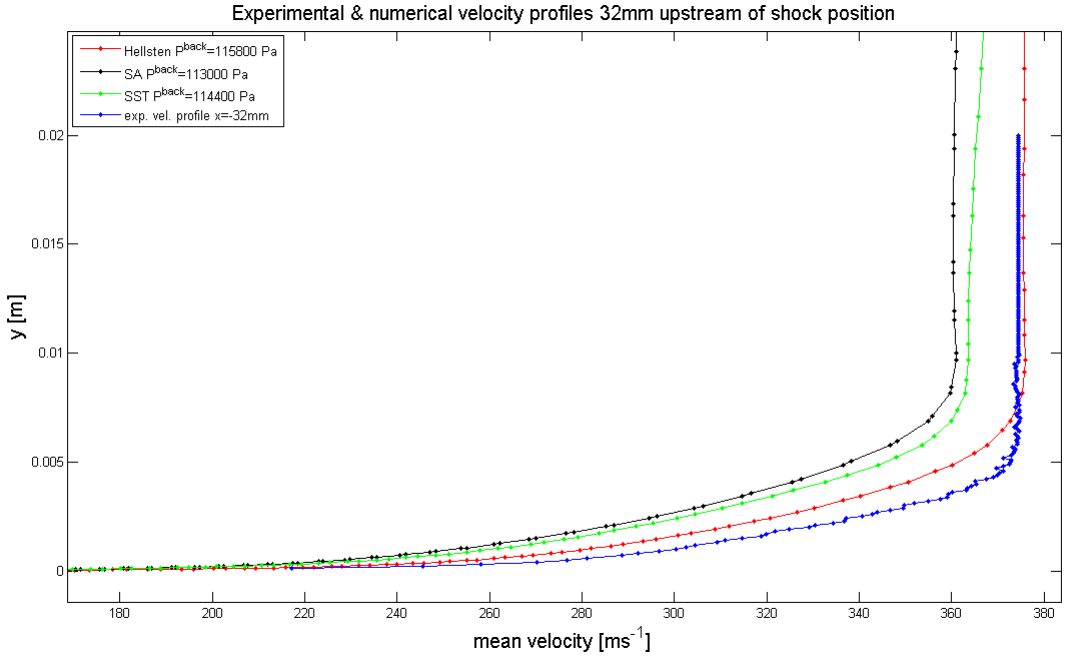

Figure 11: Comparison of velocity profiles for $M = 1.3$ at x $= 32mm$ upstream of shock position

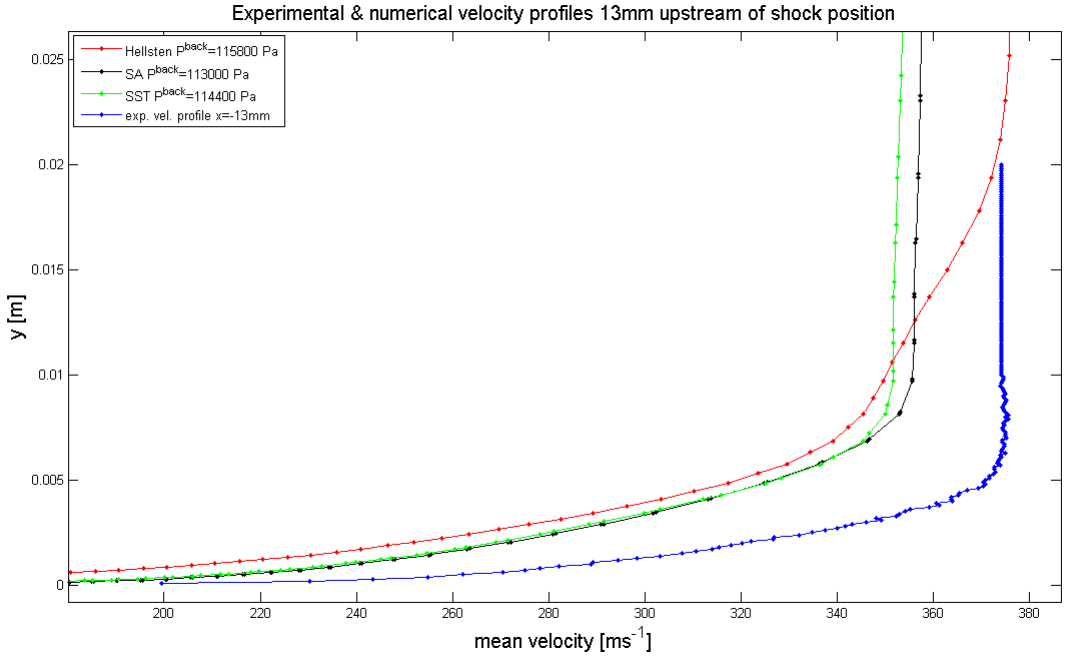

Figure 12: Comparison of velocity profiles for $M = 1.3$ at x = $13mm$ upstream of shock position

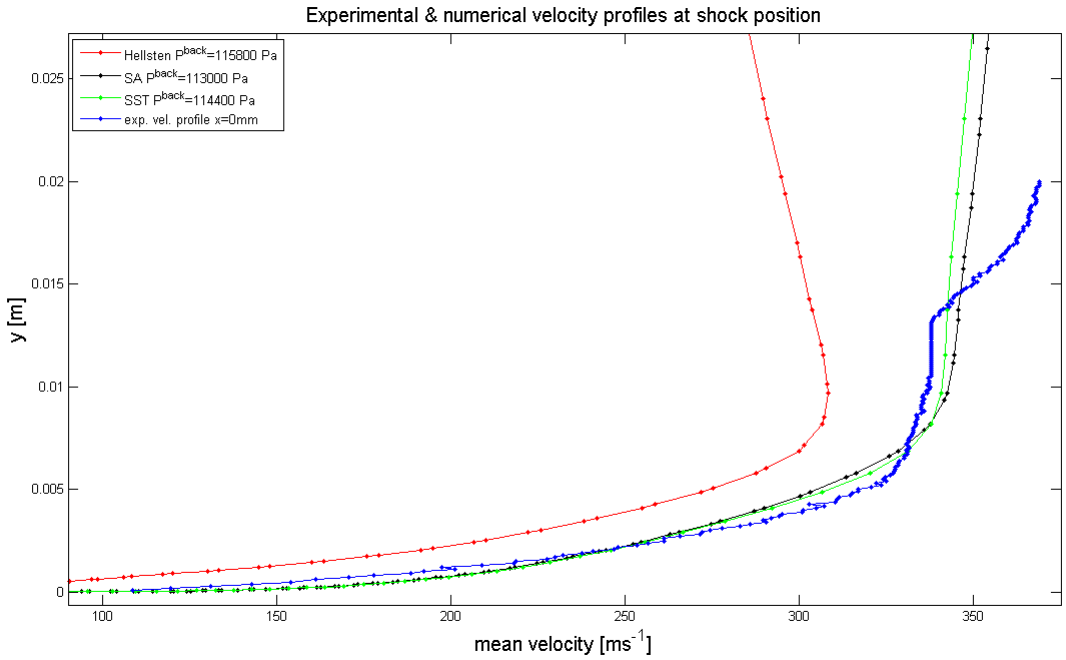

Figure 13: Comparison of velocity profiles for $M = 1.3$ at shock position

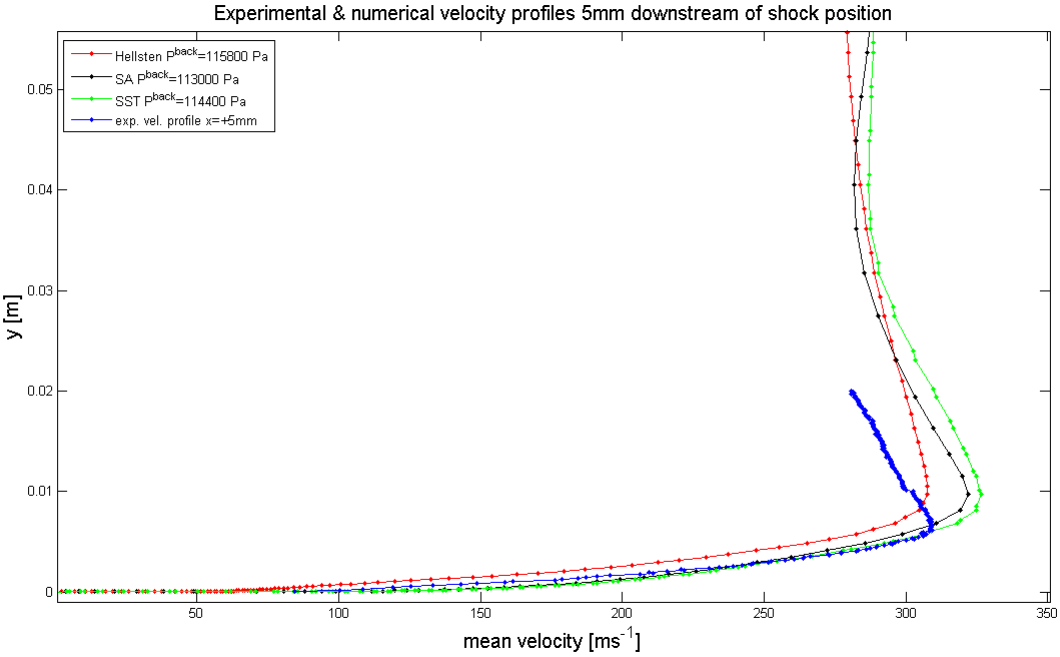

Figure 14: Comparison of velocity profiles for $M = 1.3$ at x $= 5mm$ downstream of shock position

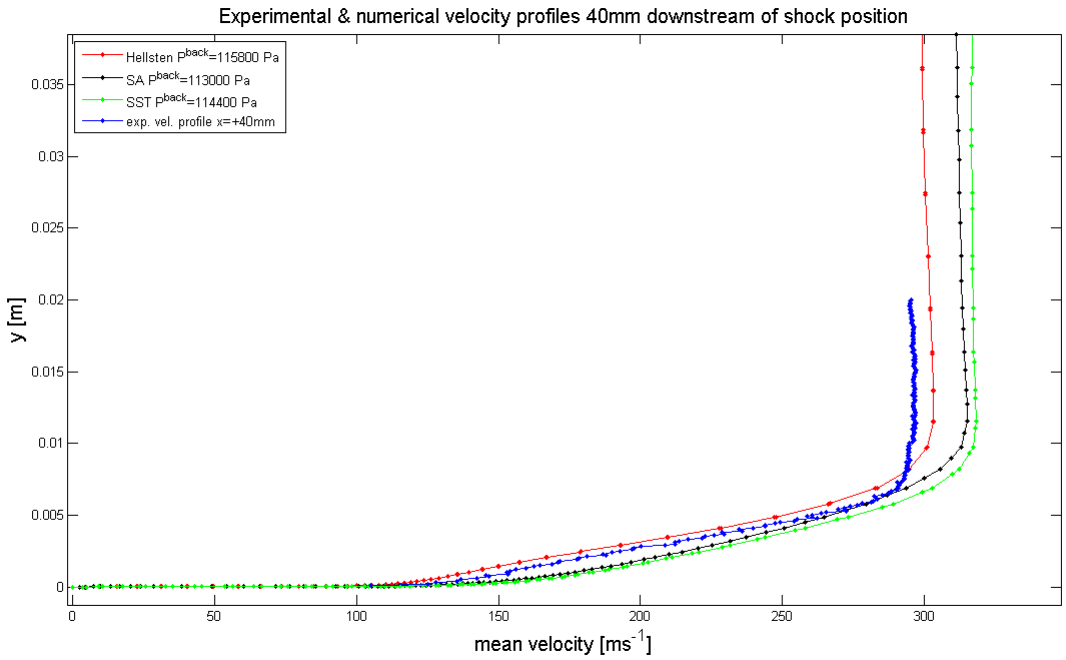

Figure 15: Comparison of velocity profiles for $M = 1.3$ at x $= 40mm$ downstream of shock position

For $M = 1.4$, the interaction velocity profiles display a trend of increasing under-prediction of the velocity when going from a distance of $30mm$ to $10mm$ upstream of the shock location. The former position shows an under-prediction of the velocity close to the wall and a slight over-prediction when approaching the free stream region for both the PDH and Wilcox models, with the Wilcox model consistently predicting a greater magnitude of the velocity than the PDH model, as can be seen in Fig. 16 for $x = -30mm$. However, at $15mm$ upstream of the shock, the velocity is under-predicted at all points evaluated and the two models give a very similar prediction. At $10mm$ upstream, Fig. 17, the agreement is fairly bad. At the position of the shock itself, the agreement for both models is rather good, as can be seen in Fig. 18. Close downstream of the shock, good agreement to experimental data is seen close to the wall for both models, with an under-prediction of the velocity ensuing further from the wall and finally an over-prediction of the free stream velocity. At $10mm$ downstream, Fig. 19, the velocity is over-predicted in the closest wall region, then under-predicted further away and finally over-predicted in the free stream

for both models, which show similar predictions, apart from the PDH model giving a larger over-prediction of the free stream velocity. This trend keeps on for points further downstream, only that the error in predicting the free stream velocity decreases for both models. An example of the profiles at the final interaction measurement point at $40mm$ downstream is seen in Fig. 20.

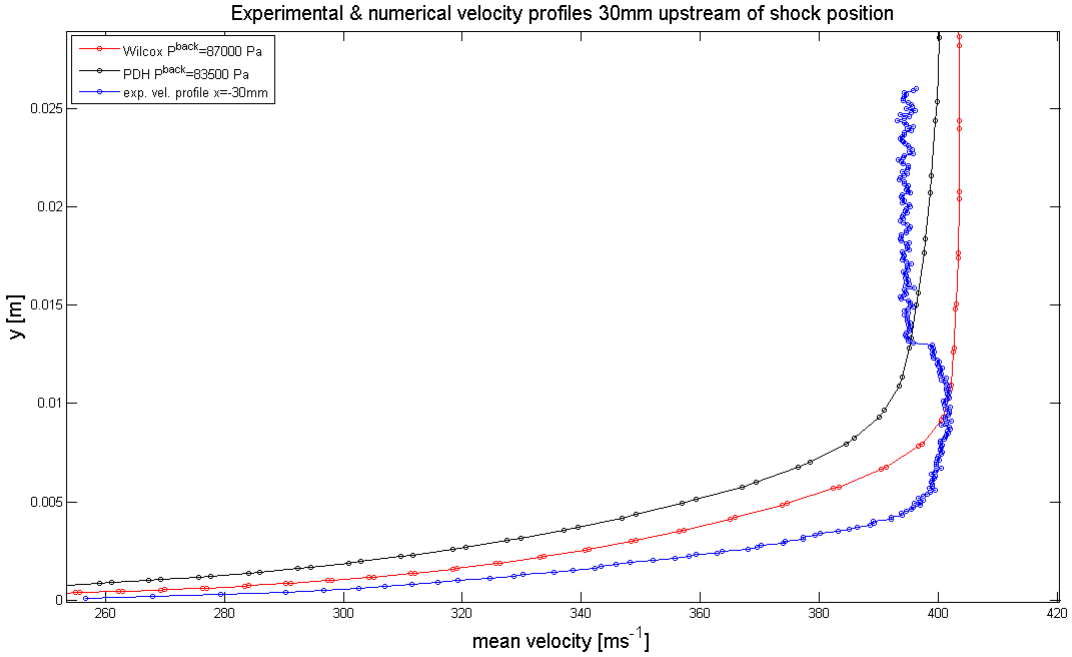

Figure 16: Interaction velocity profiles for $M = 1.4$, $30mm$ upstream of the shock position

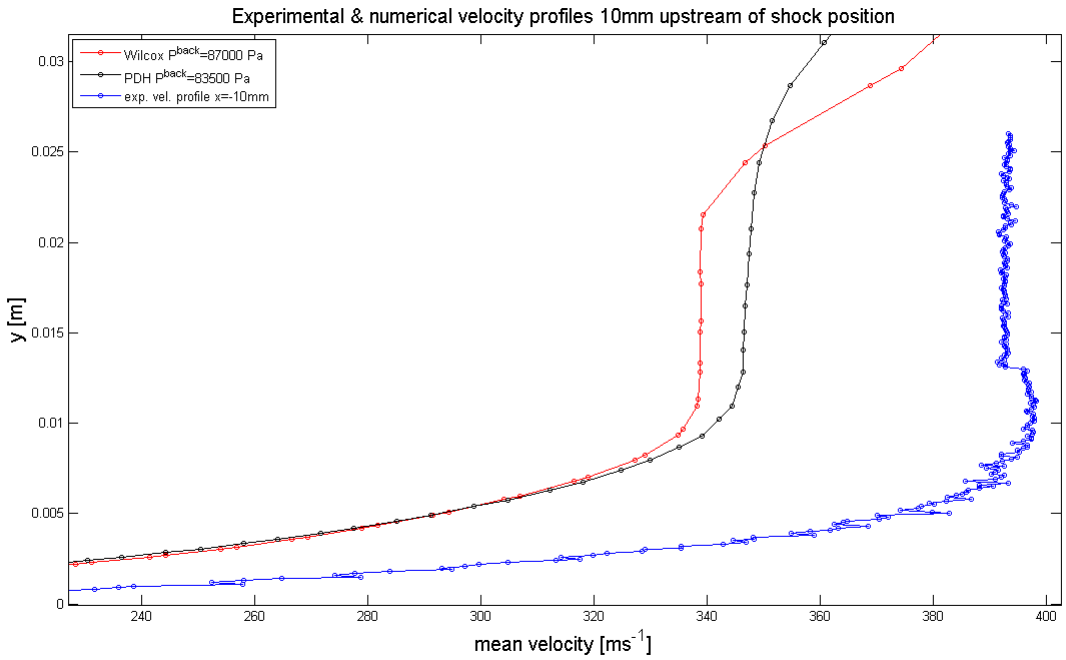

Figure 17: Interaction velocity profiles for $M = 1.4$,$10mm$ upstream of shock position

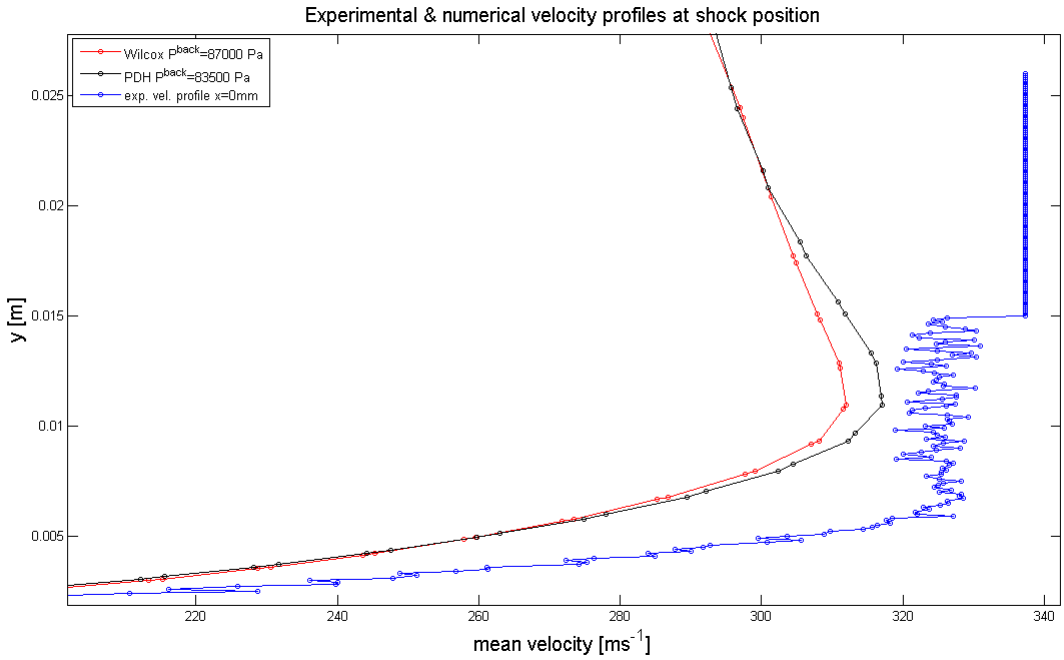

Figure 18: Interaction velocity profiles for $M = 1.4$, at shock position

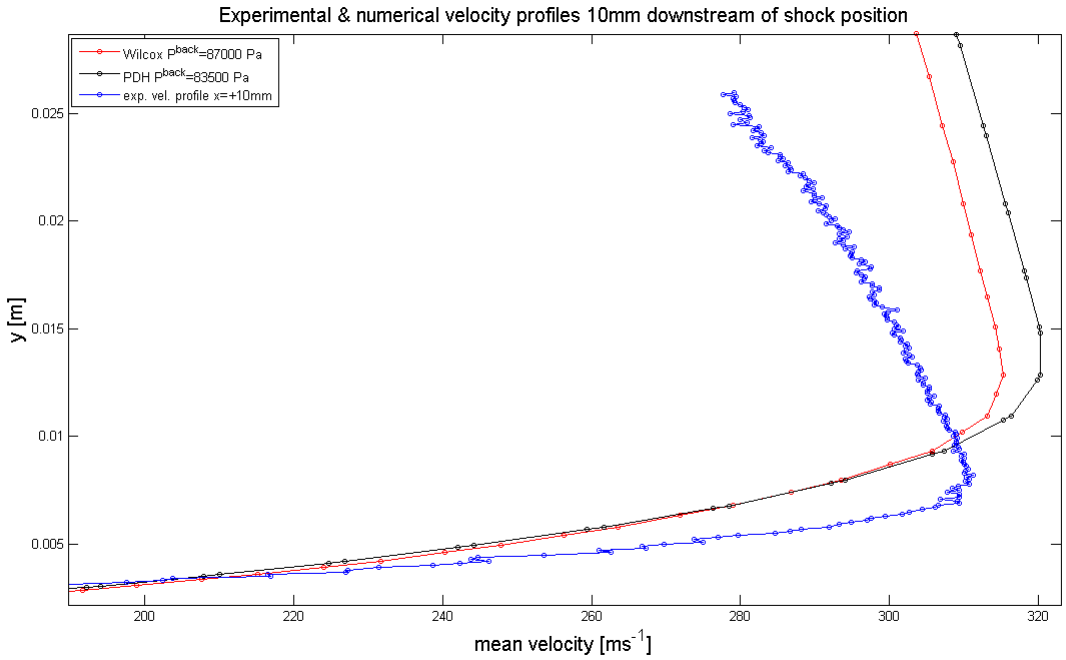

Figure 19: Interaction velocity profiles for $M = 1.4$, $10mm$ downstream of shock position

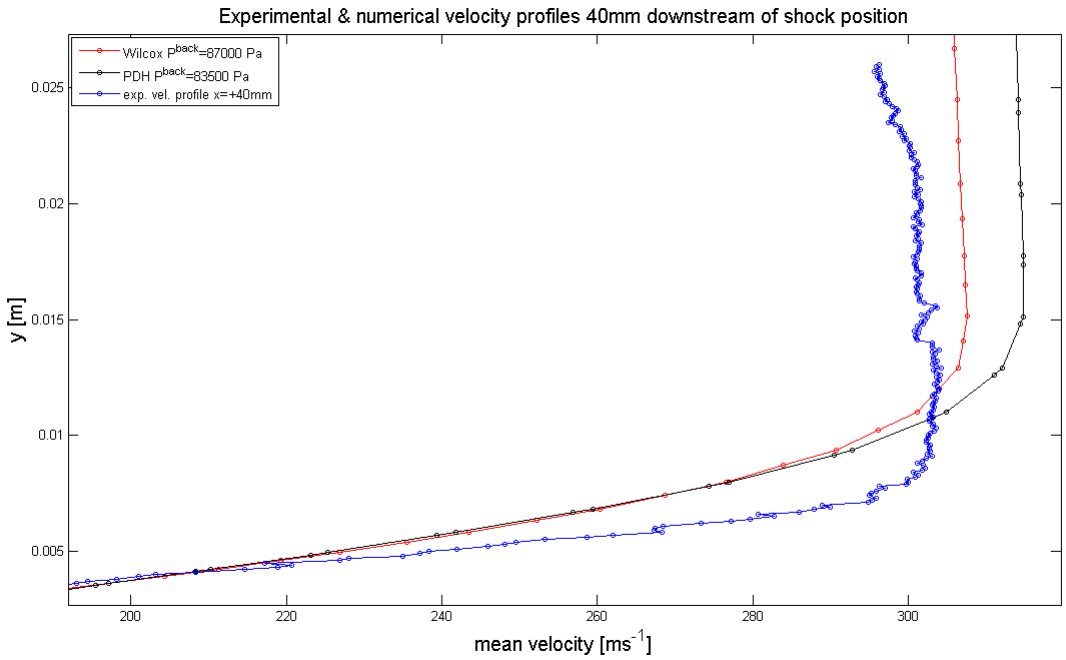

Figure 20: Interaction velocity profiles for $M = 1.4$, $40mm$ downstream of shock position

5.4 Pressure distributions

Experimental data on pressure distributions along the duct floor center-line are available for all Mach numbers investigated. Thus, corresponding profiles have been extracted for all cases presented in Table 3. For $M = 1.3$, Fig. 21 displays the predicted pressure profiles for the Hellsten, SST and SA models as compared to the experimentally obtained profile. It can be seen that the SST and SA models better agree with the experimental pressure profile, although none of the models correspond very well to it. Obviously, the Hellsten model predicts a much larger pressure gradient within the region of the shock than is suggested from experimental data. However, all models evaluated here for $M = 1.3$ seem to over-predict the rate of increase in pressure over the interaction region, despite agreeing fairly well on the pressure levels before and after the shock position.

Correspondingly the profiles for $M = 1.4$ with the PDH and Wilcox models are to be seen in Fig. 22. Here, none of the models reliably retains the experimental pressure distribution (section 3.2.4).

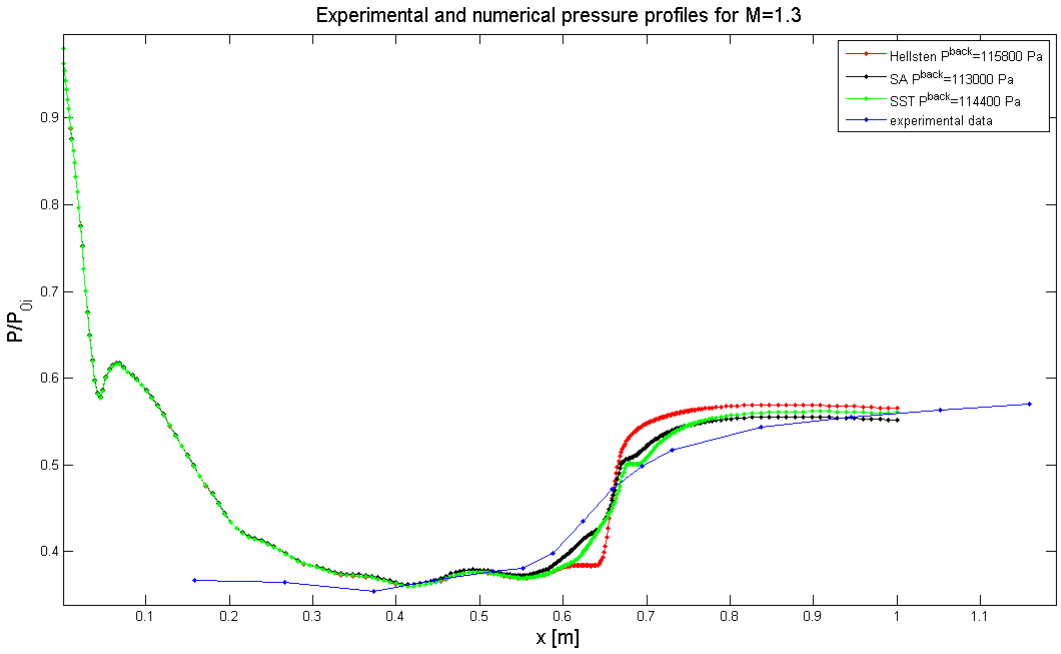

Figure 21: Pressure distributions along bottom geometrical center line for $M = 1.3$

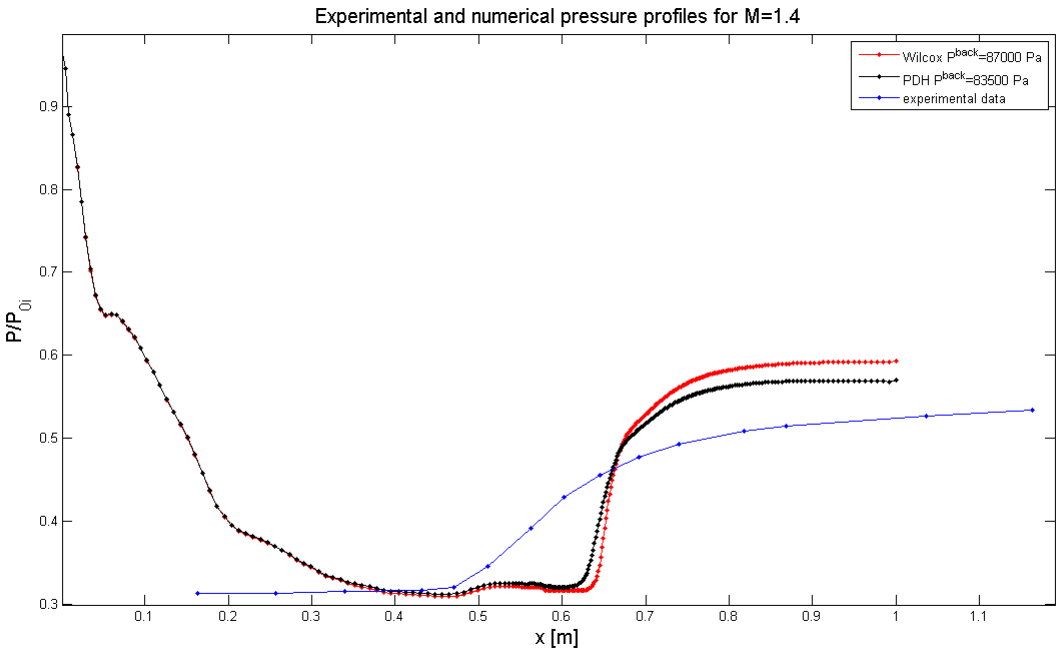

Figure 22: Pressure distributions along bottom geometrical center-line for $M = 1.4$

5.5 Shock-Induced Flow Separation

One of the great challenges for the test case is to accurately predict the separation of the flow due to the shock wave-boundary layer interactions and the corner recirculation regions. Thus, for all models tested, the results with correct back pressure (giving a shock position as close to the experimental one as possible) have been post-processed so as to detect any separation bubbles. This has been done for two-dimensional views of the top, bottom, $z = z_{min}$ and $z = z_{max}$ wall boundaries, in addition to a cross-dimensional view of the duct from the positive x-direction at the position of the shock. From the cross-sectional view, any asymmetry of the flow at the position of the shock can be detected.

Starting with $M = 1.3$, the Hellsten $k-\omega$ model, the SA model and Menter SST $k-\omega$ model have been evaluated. When it comes to the results for the Hellsten model, no corner separation bubble was observed on the top, bottom, $z = z_{min}$ or $z = z_{max}$ wall boundary, and neither was separation detected for a plane parallel to the side walls but in the center of the duct.

For the SA model with $P^{back} = 113000Pa$, separation bubbles were detected

on all boundary walls in the crossings with the adjacent walls. An example for the wall at $z = z_{max}$ can be seen in Fig. 25.

Also for the SST model, corner separation was detected for all boundary walls and an example can be seen in Fig. 26.

5.6 Corner separation

In order to detect corner separation, cross-sectional views of the duct flow field from the positive streamwise direction have been investigated. As can be seen in Fig. 23 for $M = 1.3$, the SA and SST models show clearly separated flow in all corners at the position of the shock, whereas the Hellsten model does not. Correspondingly Fig. 24 show corner separation for both the PDH and the Wilcox models at $M = 1.4$. Also, the separation bubbles as seen from a two-dimensional view of the bottom, top and side walls respectively have been considered and an average of x-wise (streamwise) extension and depth of each final solution has been calculated as follows in Table 4. For the x-wise extension, zero indicates the position of the shock and plus and minus mean downstream and upstream of it respectively.

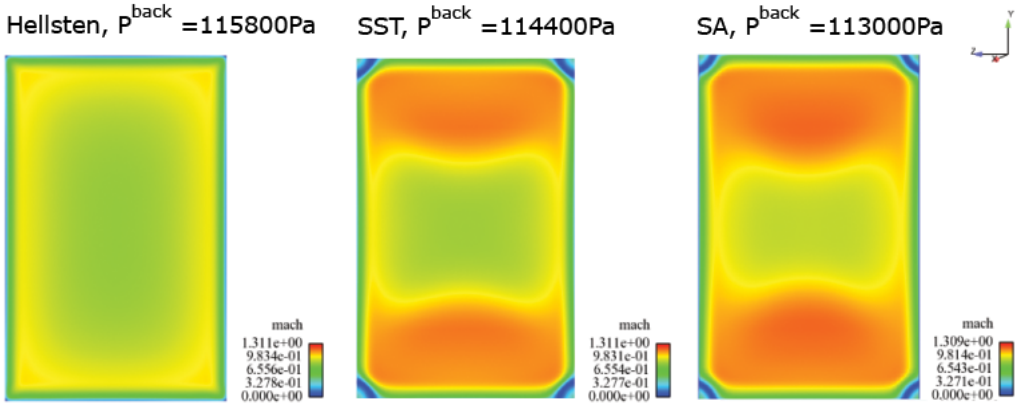

Figure 23: Cross-sectional $M = 1.3$ surfaces at shock position

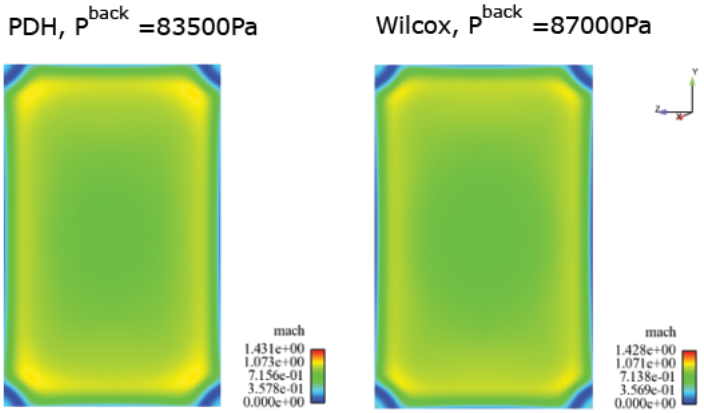

Figure 24: Cross-sectional $M = 1.4$ surfaces at shock position

Model	**Hellsten**	**SA**	**SST**	**PDH**	**Wilcox**
Mach	1.3	1.3	1.3	1.4	1.4
Separation bubble extent [mm]	-	[-72, +73]	[-64, +70]	[-59, +59]	[-58, +67]
Separation bubble depth [mm]	-	15.8	17.3	21	16.3

Table 4: Separation bubble observations for $M = 1.3$ and $M = 1.4$

Figures of velocity skin-friction patterns for the solutions to the SA model with back pressure $113000Pa$ (Fig. 25) and the SST model with back pressure $114400Pa$ (Fig. 26) are as displayed. Note that the velocity on the wall surface is zero, and thus no streamlines are seen on this surface. In contrast to these results, the two-dimensional views of the boundaries for the Hellsten case with $P^{back} = 115800Pa$, reveals no separation bubble on any surface. Thus, it seems that the Hellsten model for this case gives a poor prediction of eventual separation of the flow.

Both for the SA and SST models, clear separation bubbles are seen along the bottom lines as is obvious from Fig. 25 and 26. This is the case also for

the top and side walls and the extension and depth of the bubbles, as well as their locations, is fairly consistent for each of the respective models. Thus, for the same flow case and the same numerical settings apart from the turbulence model used, the SA and SST models seem to predict a substantially increased degree of flow separation.

Similarly, for $M = 1.4$, the solution of the PDH model with back pressure $83500Pa$ can be seen in Fig. 27 and that of the Wilcox model with back pressure $87000Pa$ in Fig. 28.

When it comes to $M = 1.4$, separation bubbles are present along all boundaries for both the PDH (bottom surface in Fig. 27) and the Wilcox models (bottom surface in Fig. 28). Both models predict fairly symmetric separation bubbles for all four corners. This is in contrast to the smeared solutions for the SA and SST models at $M = 1.4$. Notably, the presence of asymmetries in the flow has earlier been described [20] as one of the major challenges in predicting this particular flow.

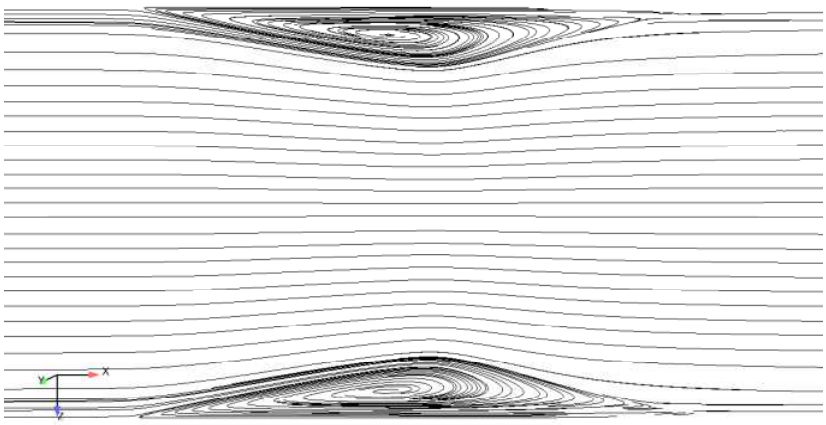

Figure 25: Skin-friction pattern on the bottom wall for SA model $P^{back} = 113000Pa$, $M = 1.3$

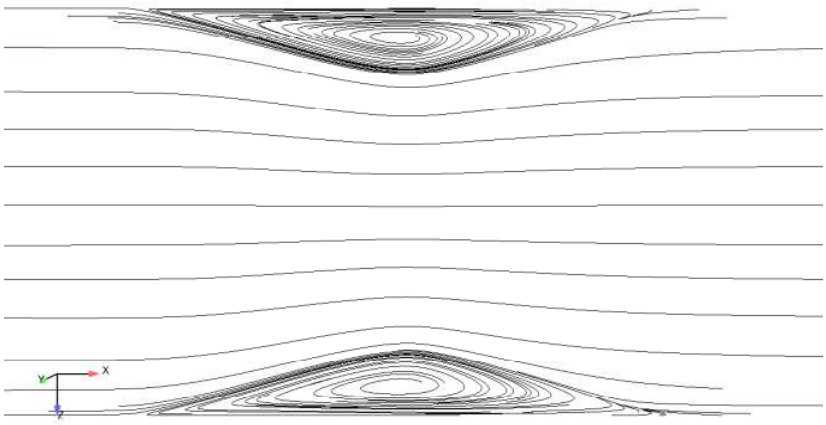

Figure 26: Skin-friction pattern on the bottom wall for SST model $P^{back} = 114400Pa$, $M = 1.3$

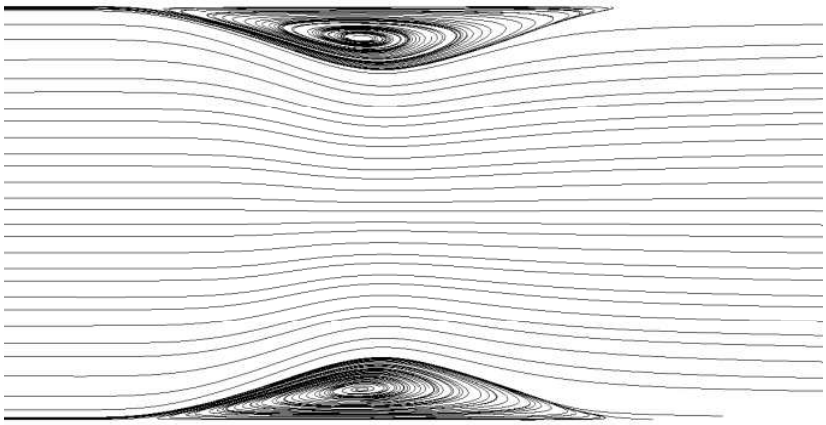

Figure 27: Skin-friction pattern on the bottom wall for PDH model $P^{back} = 83500Pa$, $M = 1.4$

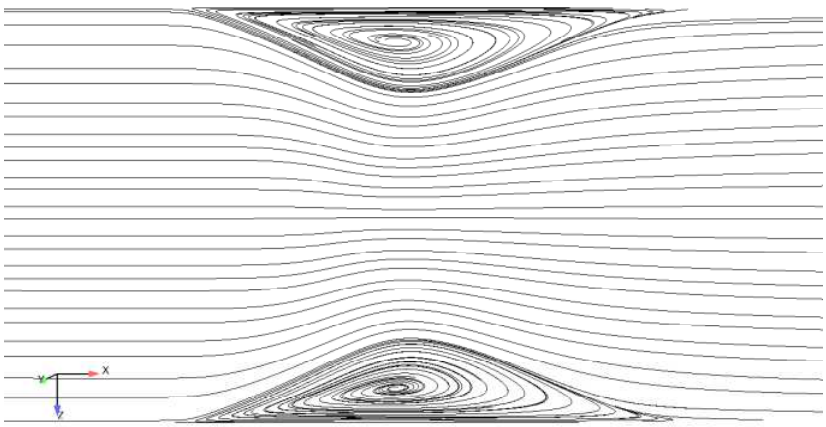

Figure 28: Skin-friction pattern on the bottom wall for Wilcox model $P^{back} = 87000Pa$, $M = 1.4$

5.7 Strong versus weak adiabatic wall boundary conditions

For all parts of the investigation, strong adiabatic boundary conditions have been used for top, bottom and side walls of the duct. The main reason is their corresponding better to the flow physics, as discussed in section 3.3. Nevertheless, comparisons between the results using strong and weak boundary conditions for a particular case have been performed. The solution considered is that of the Hellsten model with $M = 1.3$ and back pressure $P = 115800Pa$. Two successive solutions corresponding to increasing level of convergence for each boundary condition specification respectively have been assessed and the results can be seen in Fig. 29. Firstly, it is obvious that for similar CPU time, the level of convergence using weak adiabatic wall boundary conditions is roughly an order of magnitude better than for strong boundary conditions. Secondly, the movement of the shock position with respect to absolute level of convergence is smaller using weak boundary conditions than strong ones. However, sufficient data for assessing whether this would be the case when it comes to the level of convergence in relative terms has not been obtained, due to limitations in computational resources. Thus the main conclusion to be drawn from

this comparison is, that the use of weak wall boundary condition has enabled a faster convergence rate for the Hellsten model at $M = 1.3$ than with strong wall boundary conditions. Nonetheless, it is observed that the shock location may shift slightly in the predictions with the two different wall boundary conditions. Thereby not said the accuracy of the solution is more reliable as further work would be necessary for such an analysis.

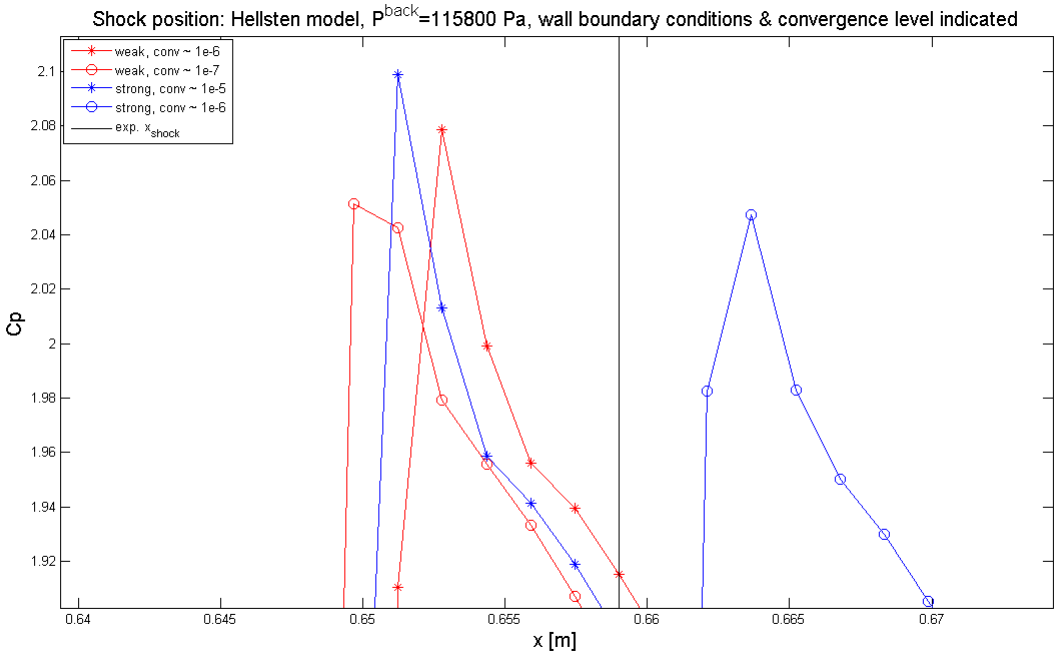

Figure 29: Shock position with weak & strong boundary conditions and the maximum level of convergence indicated in brackets for the Hellsten model with $P^{back} = 115800Pa$, $M = 1.3$

6 Conclusions

6.1 Agreement between numerical and experimental results

For the pressure distributions at $M = 1.3$, the agreement to experimental data, especially for the SA and SST models (Fig. 21), are reasonable. However, the predicted pressure profiles show a steeper step at the shock position, as compared to the experimental data. It is likely that the shock wave is actually

slightly oscillating in the measurement. This is seemingly implied by the oscillating velocities measured at the shock location as shown in Fig. 18. Nonetheless, the error present in the numerical predictions is more rooted in the modelling of the boundary layer approaching the shock location and of the flow features over the shock wave.

The predicted pressure distribution at $M = 1.4$ displays a stronger shock. It is more difficult to predict the flow at a higher Mach number, where the interaction between the shock and the turbulent boundary layer becomes increasingly strong. For the case of actually unsteady flows, it is hard to use steady RANS computations to capture all the flow physics of SWTBLI associated with unsteady flow motions. The deviations of the pressure profiles are in accordance with previous observations [19] that unsteady pressure loads in SWTBLI is hard to predict.

For the velocity profiles, a general trend is an increasing discrepancy between experimental and numerical data when approaching the position of the shock, where the boundary layer thickness is over-predicted by all the models considered. The results of interaction between the boundary layer and the shock wave show, that the stronger interaction for $M = 1.4$ as compared to $M = 1.3$ is more difficult to predict. At $M = 1.4$, the SA and SST models have produced unphysically asymmetric flow features of SWTBLI in terms of the flow separation. For both $M = 1.3$ and $M = 1.4$, there is a tendency of under-predicting the velocity upstream of the shock, within the interaction region and beyond the near wall region, whilst over-predicting it downstream of the shock. In summary, the inconsistencies between numerical and experimental results are believed to be most due to the modelling of turbulent flow physics.

It is noted, that this investigation could by no means be claimed to be an evaluation of different turbulence models in the Edge software. The main reason is that only one type of flow has been studied, with several benchmarking flow fields being essential for a turbulence model performance comparison [37]. Moreover, in order to conclude anything about the turbulence models as compared to experimental data, one must be certain that the experimental errors are significantly smaller than the modeling ones [37].

6.2 Flow features

In contrast to the other turbulence models, the Hellsten model did not predict any noticeable separation of the flow in the corners (see Fig. 23). A possible

explanation might be that this model has shown applicability only for mildly separated flows [17] and therefore strong interactions of the type studied here could actually be out of its scope. This is surprising because this model has incorporated an explicit algebraic formulation for the turbulent Reynolds stresses [36], by which the corner flow separation should have been better represented than by other linear eddy viscosity models. Worth mentioning, though, is that the Hellsten model, as well as the SA and SST models, for $M = 1.3$ gave a symmetric flowfield (Fig. 23).

It has been proved very difficult and time-consuming to predict the position of the shock according to experimental data. The approach of adjusting the back pressure revealed by no means a linear relationship. This adds to the impression of the flow case involving substantial amounts of complicated physics.

For this investigation, the flow is assumed fully turbulent. However, researchers [19] have indicted the need of accurately understanding the laminar-turbulent transition. Thus it might be possible that there are flow features apart from those of the turbulence itself, that must be more examined. This somehow gives an indication of there being a lot of uncertainties concerning the physical modeling of the flow, which really have to be sufficiently reduced in order to justify any reasoning about the performance of the turbulence models investigated [37]. In addition, it seems very difficult to evaluate turbulence models with a flow including SWTBLI, which cannot be easily predicted nor is very well understood.

6.3 Numerical issues

Once finding a reasonable back pressure for the desired position of the shock, it was realized that the position changed as the level of convergence improved. As the shock may shift sensibly with the solution convergence, it is important to drive the residuals reduced sufficiently in order to get reliable prediction. Furthermore, weak wall boundary conditions proved to give an upstream displacement with improved convergence level, in contrast to strong boundary conditions. As the convergence rate using weak boundary conditions was overall faster, this observation is believed to strengthen the assumption of strong boundary conditions solutions not being sufficiently converged. The convergence rate using weak wall boundary conditions was overall faster. However, strong wall boundary conditions were chosen in most of computations presented.

The second-order central differencing scheme introduces less artificial dis-

sipation than a second-order upwind scheme. Nevertheless, the necessity to minimize numerical errors cannot be considered as fulfilled. Thus, it would be interesting to conduct a grid-convergence study, so as to explore the dependency of the results upon the grid. Another issue is that of choosing the correct boundary conditions for truly representing the flow field in the experimental set-up [37]. This has to be pointed out as a possible source of uncertainty in the present investigation.

6.4 Outlook and recommendations

One of the major concerns has been to locate the shock in accordance with experimental results. It would be interesting to further investigate, in numerical simulations, the relation between the back pressure (at the outflow section) and the shock position at different Mach numbers. Moreover, it is recommended to perform unsteady computations analysis for the flow, particularly at $M = 1.4$. The same boundary conditions could be used in order to investigate if the case at hand is actually unsteady, so explaining the difficulties of capturing the flow behavior with steady models. Additionally, time-dependent boundary conditions should be used as experimental data for such a case is available.

Another interesting point is the feature of large-scale, low frequency shock motion as observed by many authors [19]. Currently there are discussions as to whether this is an inherent feature of the flow, or if it is rather due to the experimental set-up [21] and thus only present in wind tunnel environments. To recapitulate, further studies are needed in the area, both experimental and numerical ones.

References

[1] *Unsteady shock wave dynamics*, **P.J.K Bruce, H. Babinsky**, 2008, J. Fluid Mech, vol. 603, pp. 463-473

[2] *An experimental and numerical study of an oscillating transonic shock wave in a duct*, **P.J.K. Bruce, H. Babinsky, B. Tartinville, Ch. Hirsch**, 2010, to be presented at 48th AIAA Aerospace Sciences Meeting, Orlando, Florida, USA.

[3] *Shock wave boundary layer interaction*, **A. Hadjadj, J-P. Dussauge**, 2009, Shock Waves, Vol. 19, pp. 449-452

[4] *Investigation of the Instantaneous 3D Flow Organization of a Shock Wave/Turbulent Boundary Layer Interaction using Tomographic PIV*, **R.A. Humble, G.E. Elsinga, F. Scarano and B.W. van Oudheusden**, 2007, 37:th AIAA Fluid Dynamics Conference and Exhibit, Miami

[5] *Reynolds Stress Transport Modeling of Shock-Induced Separated Flow*, **L. Davidson**, 1995, Computers & Fluids, Vol. 24, No. 3, pp. 253-268

[6] *Investigation of a hypersonic crossing shock wave/turbulent boundary layer interaction*, **N. Narayanswami, D.D. Knight and C.C. Horstman**, 1993, Shock Waves, Vol. 3, pp. 35-48

[7] *Application of the Scaling Law for Swept Shock/Boundary-Layer Interactions*, **Y. Lee**, 2003, KSME International Journal, Vol. 17, No. 12, pp. 2116-2124

[8] *Conical Symmetry of Shock/Boundary-Layer Interactions Generated by Swept and Unswept Fins*, **G.S. Settles, F.K. Lu**, 1985, AIAA Journal, Vol. 23, pp. 1021-1027

[9] *Effects of micro-ramps on a shock wave turbulent boundary layer interaction*, **P. L. Blinde, R. A. Humble, B.W. van Oudheusden, F. Scarano**, 2009, ShockWaves, Vol. 19, pp. 507-520

[10] *Simulation of Transition with a Two-Equation Turbulence Model*, **D.C. Wilcox,** 1994, AIAA Journal, Vol. 32, No. 2, pp. 1192–1198

[11] *Re-assessment of the scale-determining equation for advanced turbulence models*, **D.C. Wilcox**, 1988, AIAA Journal, vol. 26, pp. 1414-1421.

[12] *A modified low-Reynolds-number $k-\omega$ model for recirculating flows,* **S.-H. Peng, L. Davidson and S. Holmberg**, 1997, ASME J. Fluids Engineering, Vol. 119, pp. 867-875.

[13] *Ten years of industrial experience with the SST turbulence model*, **Menter, Kuntz & Langtry** 2003, Turbulence, Heat and Mass Transfer 4, ©2003 Begell House, Inc.

[14] *The status of turbulence modeling for aerodynamics*, **Johnson, Menter and Rumsey**, 1994, AIAA paper pp. 1994-2226

[15] *Experimental and computational study of turbulent separating flow in an asymmetric plane diffuser*, **S. Obi, K. Aoki and S. Madsuda**, 1993 9th Symp. on Turbulent Shear Flows, Kyoto, paper pp. 305

[16] *Improved Two-Equation k-w Turbulence Models for Aerodynamic Flows*, **F. R. Menter** 1992, NASA Technical Memorandum 103975

[17] *New Advanced k-omega Turbulence Model for High-Lift Aerodynamics*, **A. Hellsten**, 2005, AIAA Journal, Vol. 43, No. 9, pp. 1857-1869.

[18] *Weak versus. Strong No-Slip Boundary Conditions for the Navier Stokes Equations*, **Q. Abbas**, **J. Nordström**, 2010, Engineering Applications of Computational Fluid Mechanics, Vol 4, No. 1, pp. 29-38

[19] *Fifty Years of Shock-Wave/Boundary-Layer Interaction Research: What's next?,* **D. S. Dolling**, 2001, AIAA Journal, Vol. 39, No. 8, pp. 1517-1531

[20] *Stepping Stone Test-Case 05: Nozzle with rectilinear, forced shock oscillation (UFAST case)*, **L. Temmerman**, 2009

[21] *Investigation of large scale shock movement in transonic flow*, **C. Wollblad**, **L. Davidson**, **L-E. Eriksson**, 2010, International Journal of Heat and Fluid Flow, Vol. 31, No. 4, pp. 528-535

[22] *Dependence between the shock and the separation bubble in a shock wave boundary layer interaction*, **J-F. Debiève**, **P. Dupont**, 2009, *IUTAM Synopsium on Unsteady Separated Flows and their Control*, [editors] M. Braza, K. Hourigan, Springer Netherlands.

[23] *Comparison of three large-eddy simulations of shock-induced turbulent separation bubbles*, **E. Touber, N.D. Sandham**, 2009, Shock Waves, Vol. 19, No. 6, pp. 469-478

[24] *Investigation by particle image velocimetry measurements of oblique shock reflection with separation*, **P. Dupont**, **S. Piponniau**, **A. Sidorenko**, **J.F. Debiève**, 2008, AIAA J. Vol. 46, No.6

[25] *Effect of dimples on glancing shock wave turbulent boundary layer interactions*, **K. Kontis, C. Lada, H. Zare-Behtash**, 2008, Shock Waves, Vol. 17, No 5, pp. 323-335

[26] *Three-Dimensional Turbulent Interactions Caused by Assymetric Crossing-Shock Configurations*, **D.V. Gaitonde**, **J.S. Shang**, **T.J. Garrison**, **A.A. Zheltovodov**, **A.E. Maksimov**, 1999, AIAA Journal, Vol. 37, No. 12, pp.1602-1608.

[27] *Numerical Investigation of New Topologies in Strong Crossing-Shock - Wave/Turbulent Boundary-Layer Interactions*, **J.D. Schmisseur**, **D.V. Gaitonde**, 2000, AIAA Paper 2000-0931

[28] *Shock Wave Boundary Layer Interactions in High Mach Number Flows. A Critical Survey of Current Numerical Prediction Capabilities*, **D.D. Knight**, **G. Degrez**, 1998, Advisory Rept. 319, AGARD, Vol. 2, pp. 1.1-1.35

[29] *Shock-Waves/Turbulent Boundary-Layer Interactions: Fundamental Studies and Applications*, **A. Zheltovodov**, 1996, AIAA Paper 96-1977

[30] *A One-Equation Turbulence Model for Aerodynamic Flows*, **Spalart, P. R. and Allmaras, S. R.**, 1994, Recherche Aerospatiale, No. 1, pp. 5-21

[31] *Trends in Turbulence Treatments*, **Spalart, P. R.**, 2000, AIAA 2000-2306.

[32] Effective Inflow Conditions for Turbulence Models in Aerodynamic Calculations, **Spalart, P. R. and Rumsey, C. L.**, 2007, AIAA Journal, Vol. 45, No. 10, pp. 2544-2553

[33] *Validation of the Spalart-Allmaras Turbulence Model for Applications in Hypersonic Flows*, **R. Paciorri, W. Dieudonné, G. Degrez, J.M. Charbonnier, H. Deconinck**, von Karman Institute for Fluid Dynamics, Sint-Genesius-Rode, Belgium

[34] *A two-equation turbulence model for wall-bounded and free-shear flows*, **Wilcox, D.C.**, 1993 AIAA 24th Fluid Dynamics Conference; Orlando, FL; July 6-9

[35] *Development and application of Spalart-Allmaras one equation turbulence model to three-dimensional supersonic complex configurations*, **S. Deck, P. Duveau, P. d'Espiney, P. Guillen**, 2002, Aerospace Science and Technology 6, 171-183

[36] *An explicit algebraic Reynolds stress nodel for incompressible and compressible turbulent flows*, **Wallin, S., Johansson, A. V.**, 2000, Journal of Fluid Mechanics 403, pp. 89-132

[37] A perspective on turbulence models for aerodynamic flows, D.W. Zingg, P. Godin, 2009, International Journal of Computational Fluid Dynamics, Vol. 23, No. 4, pp. 327-335

[38] http://www.foi.se/FOI/templates/Page____4568.aspx

[39] http://www.foi.se/upload/projects/edge/documentation-latest/edge-user.pdf